Optical Time-Domain Quantum State Tomography on a Subcycle Scale

Emanuel Hubenschmid,[1,*] Thiago L. M. Guedes,[1,2,3,†] and Guido Burkard[1,‡]

[1]*Department of Physics, University of Konstanz, D-78457 Konstanz, Germany*
[2]*Institute for Quantum Information, RWTH Aachen University, D-52056 Aachen, Germany*
[3]*Peter Grünberg Institute, Theoretical Nanoelectronics, Forschungszentrum Jülich, D-52425 Jülich, Germany*

(Received 24 July 2023; revised 15 May 2024; accepted 12 September 2024; published 5 November 2024)

Following recent progress in the experimental application of electro-optic sampling to the detection of the quantum fluctuations of the electromagnetic-field ground state and ultrabroadband squeezed states on a subcycle scale, we propose an approach to elevate broadband electro-optic sampling from a spectroscopic method to a full quantum tomography scheme, able to reconstruct a free-space quantum state directly in the time domain. By combining two recently developed methods to theoretically describe quantum electro-optic sampling, we analytically relate the photon-count probability distribution of the electro-optic signal to a transformed phase-space quasiprobability distribution of the sampled quantum state as a function of the time delay between the sampled midinfrared pulsed state and an ultrabroadband near-infrared probe pulse. We catalog and analyze sources of noise and show that in quantum electro-optic sampling with an ultrabroadband probe pulse one can expect to observe thermalization due to entanglement breaking. Mitigation of the thermalization noise enables a tomographic reconstruction of broadband quantum states while granting access to its dynamics on a subcycle scale.

DOI: 10.1103/PhysRevX.14.041032

Subject Areas: Optics, Quantum Physics, Quantum Information

I. INTRODUCTION

Accessing the dynamics of the quantized radiation field in free space on ultrashort timescales remains a formidable challenge even for state-of-the-art experiments [1–14]. Yet, the characterization of and control over broadband pulsed quantum states are key for the further development of quantum optics. This encompasses foundational queries on the dynamics of (nonlinear) quantum optical systems [15] and the very physicality or realizability of quantum states [16] to quantum technological applications [17,18] such as quantum communication [19–26], which require inherently multimode wave packets to transmit (quantum) information. Paving the way toward the regime of time-domain quantum optics requires the theoretical and experimental capabilities to completely characterize pulsed quantum states, a task known as (optical) quantum state tomography [4,10,14,27–39]. To this date, tomographic reconstruction is limited to quantum states of a single [1–9] up to a few [10–13] (reproducible) temporal modes, restricting the observable dynamics. We identify and address both a conceptual and a practical obstacle hindering the advancement of quantum optics toward the so-called subcycle regime—allowing the observation of quantum properties of light in the time domain with a temporal resolution below a single optical cycle of the sampled state.

Conceptually, quantum states of a broad band of modes miss a description suitable for quantum tomography. While for a few discrete modes, a quantum state can be represented by a (quasiprobability) distribution in a phase space, spanned by two conjugate quadratures of each mode, divergences complicate the direct extension to the continuum of modes [40,41]. We introduce a new family of broadband (phase-space) quasiprobability distributions capturing the dynamics of the pulsed quantum state on a subcycle timescale, as depicted in Fig. 1(a) for a coherent state.

On the practical front, there is no currently available measurement scheme capable of obtaining the complete statistics and dynamics of the broadband (phase-space) quasiprobability distribution. We propose a measurement scheme based on electro-optic sampling, able to access the broadband quasiprobability distribution together with its dynamics.

Originating as a classical time-domain spectroscopy technique, electro-optic sampling stands out by its high temporal resolution. The technique utilizes a short,

*Contact author: emanuel.hubenschmid@uni-konstanz.de
†Contact author: thiago.lucena@uni-konstanz.de
‡Contact author: guido.burkard@uni-konstanz.de

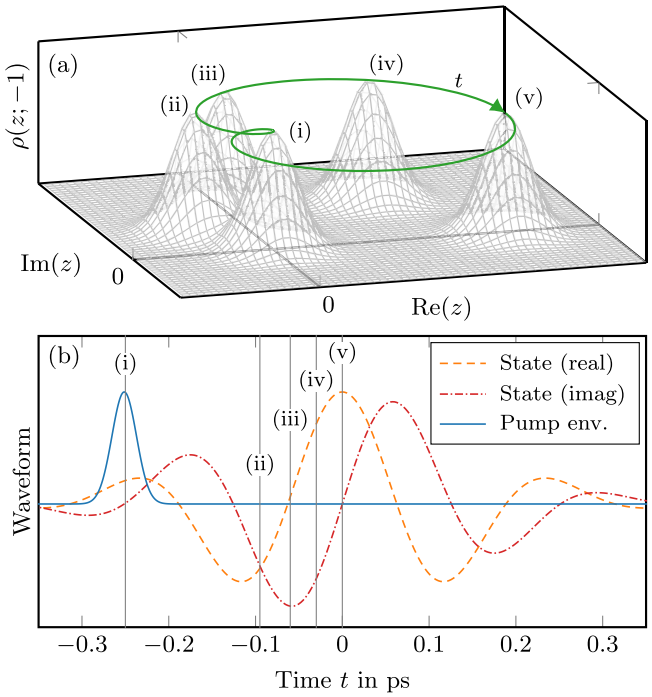

FIG. 1. The goal of time-domain quantum tomography is to reconstruct a pulsed quantum state together with its dynamics directly in the time domain. (a) Exemplary time evolution in phase space of the broadband (Husimi) quasiprobability distribution $\rho(z;-1)$ of a coherent (pulsed) quantum state, whose quadratures evolve dynamically following the solid green line. The free time evolution of the distribution starts in the vacuum at (i), spirals outwards via (ii)–(iv) until reaching maximum displacement in (v) before returning to the vacuum. (b) The corresponding sampled waveform of the pulsed quantum state with the dashed orange line (dash-dotted red line) for the real (imaginary) part. The state is sampled and thus averaged over the duration of a probe pulse envelope (solid blue line). If the probe pulse is shorter than the duration of a single cycle of the sample pulse, the measurement is said to be subcycle. For a probe pulse centered at the vertical line located at (i), the sampled waveform averaged over the duration of the probe is close to zero, while at (v) the average real part of the waveform is maximal, matching the free time evolution in (a).

higher-frequency probe pulse, usually in the near infrared (NIR), to sample a longer pulse of lower frequency, usually in the terahertz to midinfrared (MIR) range. The interaction of the low- and high-frequency electromagnetic field in a nonlinear crystal correlates the ellipticity of the higher-frequency probe with the state of the lower-frequency electric field, averaged over a small time slice defined by the duration of the probe pulse, as shown schematically in Fig. 1(b). Therefore, by measuring the change in ellipticity of the high frequencies, using a so-called ellipsometer, one can infer information about the low-frequency electric field at the time of interaction [42–61]. Besides achieving subcycle resolution, the indirect-measurement character of electro-optic sampling makes it a nondestructive measurement and enables detection in the terahertz to MIR range.

While electro-optic sampling is an established tool for time-resolved measurements of the electromagnetic-field-related Y quadrature, with applications spanning from solid-state research [62] to the investigation of biological systems [63], the detection of the (classical) X-quadrature related conjugate of the electric field, the so-called Hilbert transform, has been demonstrated only recently [45]. The Hilbert transform of a time-dependent signal can be calculated by phase shifting the Fourier transform of the signal by $+\pi/2$ or $-\pi/2$ if the frequency is positive or negative and transforming back to the time domain. By associating the annihilation operator $\hat{a}_\omega$ of a photon with the positive frequency ω and the creation operator $\hat{a}_\omega^\dagger = \hat{a}_{-\omega}$ with the negative frequency $-\omega$, the Y-quadrature operator $\hat{Y}_\omega = (\mathrm{i}/2)(\hat{a}_\omega^\dagger - \hat{a}_\omega)$ is related to the conjugate X quadrature $\hat{X}_\omega = \frac{1}{2}(\hat{a}_\omega^\dagger + \hat{a}_\omega)$ by the frequency component of the Hilbert transform. As shown by Sulzer *et al.* [45], the two conjugate observables can be accessed using electro-optic sampling. If a half-wave plate (HWP) is used in the ellipsometry, the X quadrature is detected, while a quarter-wave plate (QWP) leads to a Y-quadrature measurement. This can be understood from the phase-space picture in Figs. 2(d)–2(g) and Figs. 2(h)–2(k) which shows the state of the probe and a quantum state (a squeezed state represented by an ellipse in phase space in this example) before and after the HWP or QWP. Both wave plates mix the two polarizations of the NIR frequencies and thus enable the phase-sensitive measurement by interfering the NIR excitations, generated by the nonlinear interaction, with the probe pulse. We will refer to the probe as local oscillator (LO) in the context of the ellipsometry and represent it as a vector in phase space, since fluctuations can be neglected compared to its amplitude. Yet, the QWP introduces $\pm\pi/2$ and the HWP π or 2π relative phase shifts between the LO and the quantum state, which leads to the measurement of orthogonal quadratures (X and Y). While straightforward for monochromatic modes, the intricacy in detecting the conjugate observables for free-space pulses originates from the joint contribution of sum-frequency generation (SFG) and difference-frequency generation (DFG) to the nonlinear interaction. By detecting the complete spectrum of the NIR excitations, the SFG and DFG contributions can interfere and lead to a degradation of the X-quadrature signal. The interference can be avoided by selecting the appropriate frequency band after the nonlinear interaction, favoring either SFG or DFG [45]. The ability to measure (classical) conjugate observables makes electro-optic sampling a prominent candidate for quantum state tomography in the time domain. We propose to detect the two conjugate variables simultaneously by splitting the filtered NIR frequencies into two neighboring frequency bands which can be used to perform a QWP and HWP measurement simultaneously, as schematically shown

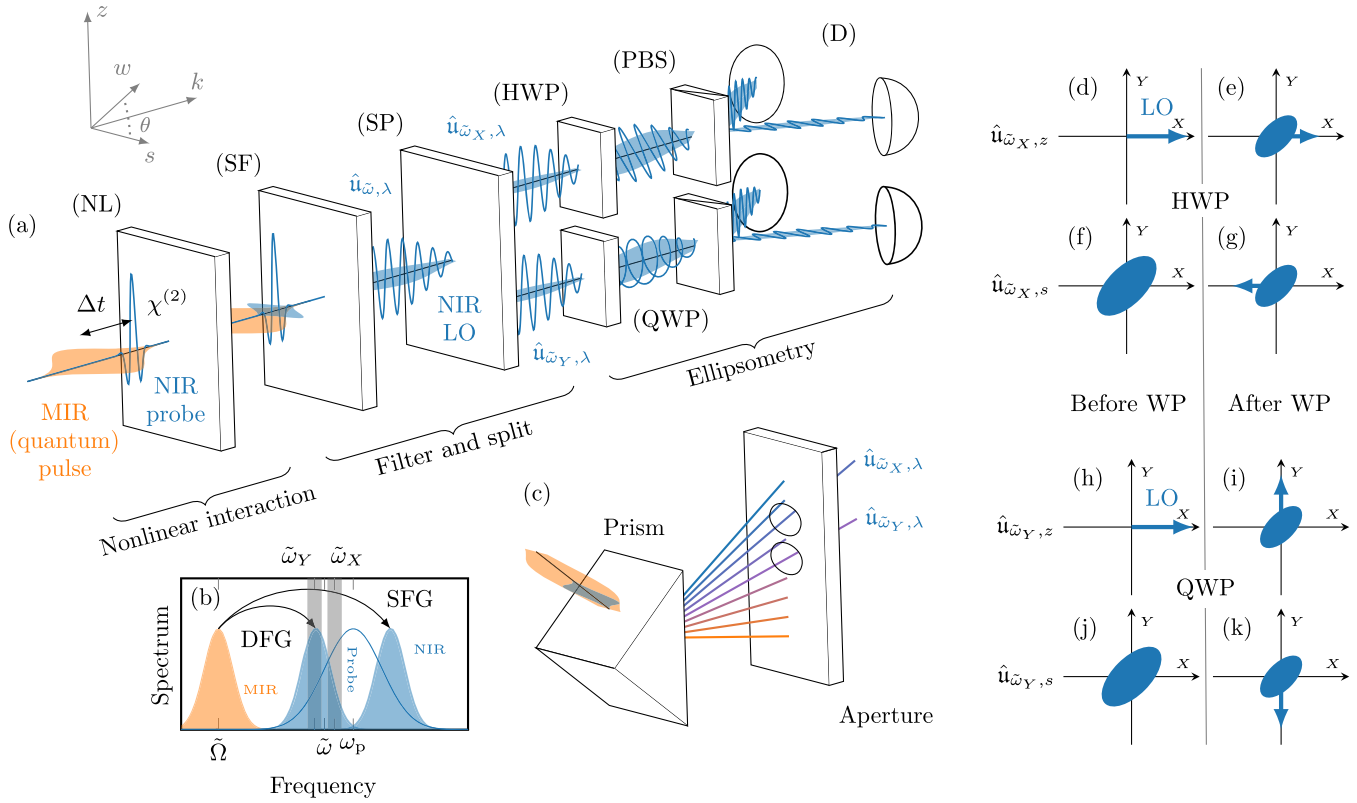

FIG. 2. (a) Schematic of the proposed electro-optic quantum tomography setup. The z-polarized near-infrared (NIR) probe pulse interacts with the s-polarized midinfrared (MIR) temporal mode in the zinc-blende-type nonlinear crystal, labeled (NL), and generates new excitations in the s-polarized NIR modes. By varying the relative time delay Δt between the NIR pulse and the pulsed MIR mode, the MIR mode is sampled. The s- and z-polarized NIR modes then undergo a spectral filter station, labeled (SF), resulting in a narrow (quasimonochromatic) frequency band $\bar{\omega}$ defining a mode $\hat{\mathbf{u}}_{\bar{\omega},\lambda}$ (for each polarization $\lambda = s, z$). The quasimonochromatic mode is then split (SP) into two modes $\hat{\mathbf{u}}_{\bar{\omega}_X,\lambda}$ and $\hat{\mathbf{u}}_{\bar{\omega}_Y,\lambda}$, each being directed toward one detection stage. At each detection stage $i \in I = \{X, Y\}$ the NIR excitations together with the filtered probe, which now assumes the function of a local oscillator (LO), pass through a φ_i wave plate rotated by an angle θ_i, labeled (WP). Afterward, the s and z components of each quasimonochromatic NIR frequency band are split spatially with the aid of a polarizing beam splitter, labeled (PBS). The photon numbers $\hat{n}_{i,s}$ and $\hat{n}_{i,z}$ in the s- and z-polarized components of each quasimonochromatic cut are counted using photodetectors, labeled (D), and the difference $\Delta\hat{n}_i = \hat{n}_{i,s} - \hat{n}_{i,z}$ constitutes the electro-optic signal. (b) Schematic representation in the frequency domain of the MIR excitation after up-conversion (shaded in blue) via sum- and difference-frequency generation (SFG and DFG, respectively). The overlap with the probe pulse (blue line) allows for the ellipsometry. The gray areas represent the filtered spectral cuts defining the mode operators $\hat{\mathbf{u}}_{\bar{\omega}_X}$ and $\hat{\mathbf{u}}_{\bar{\omega}_Y}$. (c) A possible realization of the filter and split stage. A prism spectrally decomposes the pulses and an aperture selects two narrow frequency bands. (d)–(k) Phase-space representation of the ellipsometry between the s- and z-polarized modes $\hat{\mathbf{u}}_{\bar{\omega}_{X/Y},s}$ and $\hat{\mathbf{u}}_{\bar{\omega}_{X/Y},z}$. The (classical) LO is represented as a vector, while the up-converted NIR excitations are exemplarily represented by a squeezed state. A $\theta_X = 22.5°$ rotated half-wave plate (HWP) adds a relative phase of π between the s-polarized LO pulsed quantum state, resulting in an X-quadrature measurement. A $\theta_Y = 45°$ rotated quarter-wave plate (QWP) adds a $+(\pi/2)$ $(-(\pi/2))$ relative phase between the z-polarized (s-polarized) LO and the state, detecting the Y quadrature.

in step (SP) in Fig. 2(a). The filtering and splitting can be implemented in numerous ways, e.g., using a beam splitter or a prism. In the main text we will follow the latter implementation, depicted in Fig. 2(c). The former is described in Appendix A. Alternatively, two probe pulses entering the nonlinear crystal in two different channels could be used to implement the simultaneous measurement [49–51,57–59].

So far, first steps toward the application of electro-optic sampling to quantum states have been taken. While it has already been applied to sample the fluctuations of the electromagnetic-field broadband ground state [64], as well as of ultrabroadband squeezed states in the time domain with subcycle resolution [65], it yet misses the ability to access the complete joint phase-space statistics of an arbitrary quantum state, experimentally and theoretically. We close this conceptual gap by proposing a modified quantum electro-optic sampling setup capable of measuring two noncommuting quadratures of the spatiotemporally localized MIR mode simultaneously. However, extending the theoretical machinery of a classical free-space

technique to the simultaneous quantum measurement of noncommuting observables defined over a broad frequency band, a daunting task even for few-discrete-mode systems [66], harbors a number of challenges, which we solve and present in three steps throughout this work.

First, in contrast to the classical counterpart, the simultaneous measurement of conjugate observables proves to be considerably more intricate in the quantum realm. While the achievable resolution in quantum phase space is fundamentally limited by the measurement uncertainty relations owing to the noncommutativity of conjugate observables [67–69], in practice the resolution is constrained by detection inefficiencies [37,66]. Overcoming the inefficiency requires sufficiently strong nonlinear interactions, driven by high-intensity probe pulses, something known to lead to backaction in quantum electro-optic sampling [56], making perturbative descriptions unreliable in this regime. We overcome this constraint by developing a nonperturbative theory of quantum electro-optic sampling, based on the first-order unitary introduced in Ref. [54].

Second, while the sampling of the classical conjugate observable of the electric field, i.e., its Hilbert transform, on subcycle timescales has already been demonstrated [45], measuring or even defining the conjugate variable of the electric field in the quantum regime is not a straightforward endeavor [70]. The electro-optic sampling of the X quadrature requires filtering, which poses a challenge in the quantum regime since the broadband of continuous modes becomes entangled during the nonlinear interaction. Filtering leads to the breaking of entanglement, a phenomenon known as thermalization [54], introducing noise of purely quantum origin. We propose a means to attenuate this noise by selecting an appropriate frequency band after the nonlinear interaction, thereby reducing the degradation of entanglement.

Third, we utilize the framework developed in Ref. [66] together with our nonperturbative theory of electro-optic sampling and relate the count-probability distribution of the electro-optic signal to the (transformed) broadband phase-space quasiprobability distribution. The transformation takes all the quantum effects described in the previous paragraphs into account and facilitates the mitigation of the additional quantum noise. The resulting model enables the mapping of the measurement results of multichannel quantum electro-optic sampling to phase-space information, and we demonstrate its application for optical time-domain quantum state tomography with subcycle resolution.

Our paper is structured as follows. In Sec. II we develop a theoretical model to describe quantum electro-optic sampling. Section III presents the main result of this work: the count-probability distribution of the electro-optic signal. In Sec. IV we utilize the analysis developed in the preceding sections to discuss realistic implementations of optical time-domain quantum tomography.

II. THEORETICAL FRAMEWORK

Before embarking on the formal theoretical description of our model, we develop an intuitive picture of electro-optic sampling as a quantum tomography scheme for reconstructing the quantum state of the electromagnetic field with a subcycle resolution in Sec. II A. In the subsequent sections, we then describe the formal model of our proposed generalization of quantum electro-optic sampling. We divide the measurement protocol into three stages: the nonlinear interaction (Sec. II B), the filter and split stage (Sec. II C), and the ellipsometry stage (Sec. II D). In Sec. II E we show how our model improves and generalizes the effective description of the nonlinear interaction laid down in Ref. [54].

A. Heuristics of (time-domain) quantum tomography

In optical tomography of quantum states, the reconstruction of the state is usually performed in phase space. A (single-mode) quantum state can be represented by a distribution over a complex argument, where the real part corresponds to the generalized coordinate (X quadrature) and the imaginary part to the generalized momentum (Y quadrature) of the mode. One example of such a quasiprobability distribution is the widely known Wigner function; another related example is the Husimi distribution, visualized for a broadband coherent state in Fig. 1(a) at different points of its time evolution. Over time the quasiprobability distribution of a single-mode quantum state would rotate in phase space and thus by directly measuring the photon number in that single mode, only information about the amplitude, but not about the phase, can be collected. For this reason, an ancillary mode in a coherent state of displacement β is introduced, also referred to as a local oscillator, with which the single mode can interfere. The difference counts Δn, resulting from a balanced photodetection of the interfered signal, contain information about the X or Y quadrature of the quantum state. Such a phase-sensitive measurement is called homodyne detection. If two balanced detections, $i = X, Y$, make use of local oscillators shifted by $\pi/2$ relative to each other, the tomography scheme is able to sample the quasiprobability distribution of the single mode at the (discrete) complex arguments $z(\{\Delta n_i\}) = (\Delta n_X + \mathrm{i}\Delta n_Y)/|\beta|$ [35–39]. In the case of the ellipsometry, the $\pi/2$ phase difference of the two local oscillators is achieved by the usage of a half- and a quarter-wave plate, as indicated in Figs. 2(d)–2(g) and Figs. 2(h)–2(k). Although popularly used tomography techniques such as homodyne detection make use of direct measurements, entangling the analyzed mode with ancillary modes using a nonlinear crystal implements an indirect measurement, as we have shown in Ref. [66]. In this case, the difference-count probability distribution,

$$p(\{\Delta n_i\}) \propto \rho[z(\{\Delta n_i\})/\sinh(|\zeta|); \tilde{s}], \tag{1}$$

is proportional to the $\tilde{s}$-quasiprobability distribution ρ of the quantum state in which the parameter $\tilde{s} = 1–2\coth^2(|\zeta|)$ is determined by the two-mode squeezing strength ζ of the nonlinear crystal. These distributions are a smoothed-out version of the Wigner function, which is achieved by convolving the Wigner function with a Gaussian distribution of variance proportional to $-\tilde{s}$. To ensure non-negativity of the quasiprobability distribution, one requires $\tilde{s} < -1$. With increasing squeezing strength, the measurement is made stronger and $\tilde{s}$ approaches its maximum value of -1.

If the nonlinear crystal is driven by an ultrabroadband pulse instead of a few monochromatic modes, the tomography scheme from the previous paragraph constitutes a (generalized) version of quantum electro-optic sampling. The quantum version of electro-optic sampling can be understood as indirect homodyne detection between different frequency bands and orthogonal polarizations. The nonlinear crystal, (NL) in Fig. 2(a), generates new NIR excitations correlated to the MIR quantum pulse localized to a time window defined by the probe pulse. As indicated in Fig. 2(b), the probe pulse is broadband compared to the central frequency of the MIR pulse leading to a spectral overlap between the new (s-polarized) NIR excitations and the (z-polarized) probe pulse. In a process called ellipsometry, a wave plate with its optical axis rotated by an angle θ is used to interfere the two polarization components. The balanced detection between the two polarization directions of the interfered signal reveals phase information about the NIR excitations. The function of the probe pulse in the ellipsometry can be understood as a local oscillator. By repeating this measurement for different relative time delays Δt between the high- and low-frequency pulses, the electric field can be sampled as a function of time (delay), as depicted in Fig. 1(b). In order to sample the waveform directly in the time domain, the high-frequency pulse needs to be shorter than a single optical cycle of the low-frequency pulse. If this is the case, the measurement is said to be subcycle. In principle, the same could be achieved with homodyne detection, although this would require either fast photodetectors or the local oscillator to be highly subcycle with respect to itself. The latter requirement is due to the shared frequency domain of the local oscillator and the sampled pulse in homodyne detection. The nonlinear mechanism underlying electro-optic sampling allows the high-frequency pulse to be single cycle or even a few cycles long, while retaining its subcycle character relative to the low-frequency pulse. Furthermore, electro-optic sampling provides access to the frequency range right between the gap of electronic and optical frequencies, the so-called terahertz range. Generation and detection of terahertz or even MIR frequencies using electronics or optics remain challenging. On the other hand, detection in the high-frequency range, usually spanning from near-infrared to optical frequencies, can be easily achieved using optical components. While the frequencies in this work are in the MIR at ∼25 THz and thus considered to be optical frequencies, the results transfer to even lower frequencies by adjusting the dispersion relation of the nonlinear crystal (as long as absorption is negligible).

If the probed low-frequency modes are in a quantum state, we would expect the count-probability distribution to follow the quasiprobability distribution of the quantum state averaged over the time window defined by the short probing high-frequency pulse, as sketched in Fig. 1(b). However, the subcycle nature of the high-frequency pulse has an additional quantum mechanical effect. Since the Gabor limit forces a bandwidth broadening if the pulse is made shorter [71], additional MIR modes, which are not measured by the electro-optic sampling (unsampled modes), become entangled to the sampled modes during the nonlinear interaction. Therefore, the entanglement between the sampled and unsampled modes is broken through measurement. This entanglement breakage leads to an increase of the von Neumann entropy of the sampled quantum state, which in turn creates thermal excitations [54]. The thermalization is reflected in the electro-optic signal as excess noise [see Fig. 7 and Sec. III], leading to a resolution trade-off between time and phase-space coordinates. The sampled frequencies are up-converted to the detected modes via difference-frequency generation, while the thermalized modes are up-converted by sum-frequency generation. Therefore, the excess noise due to thermalization can be mitigated by filtering in the NIR below the central frequency of the probe pulse.

B. Nonlinear interaction

Since electro-optic sampling is an indirect measurement of low-frequency modes mediated by a subcycle pulse of high-frequency ancillary modes, the two frequency ranges have to be correlated in order to access information about the former by measuring the latter. In this work we consider low-frequency midinfrared and high-frequency near-infrared modes, which interact in a zinc-blende-type nonlinear crystal of length L, refractive index n_ω [given by Eq. (C1)], and a coupling constant $d = -n_{\omega_\mathrm{p}}^4 r_{41}$ dependent on the refractive index at the central probe frequency ω_p and the second-order electro-optic (susceptibility) coefficient, $r_{41} = 4\ \mathrm{pm\,V^{-1}}$ (see Ref. [72], p. 500).

As depicted in Fig. 2, in the nonlinear crystal, the interaction of the z-polarized NIR modes with the s-polarized MIR modes generates new excitations in the s-polarized NIR modes (for details about the geometric arrangement, see Ref. [46]). This interaction can be described by the unitary time-evolution operator $\hat{U}_\mathrm{NL} = \exp(\hat{S}_\mathrm{NL})$ with [47,54]

$$\hat{S}_\mathrm{NL} = \int_{|\Omega|<\Lambda} \int_{\Lambda<|\omega|} S(\Omega,\omega)\hat{a}_{\Omega,s}\hat{a}^\dagger_{\omega,s}\mathrm{d}\Omega\mathrm{d}\omega; \qquad (2)$$

as long as the coherent probe is strong compared to any quantum contributions (including depletion), absorption is negligible (off-resonant regime) and there is no overlap between the MIR and NIR frequency ranges of interest. To ensure skew Hermiticity of $\hat{S}_{\mathrm{NL}}$, the condition $S^*(\omega,\Omega) = -S(\Omega,\omega)$ has to be fulfilled. We denote angular frequencies in the MIR range by Ω while the NIR range is represented by ω. From here on we will refer to the angular frequency as just frequency. To avoid frequency crossing between the NIR and MIR ranges, a cutoff frequency Λ is introduced. The operator $\hat{a}_{\omega,s}$ with $\omega > 0$ is the annihilation operator for the mode with frequency ω and polarization s. We use the convention $\hat{a}_{-\omega,s} = \hat{a}^\dagger_{\omega,s}$ and $[\hat{a}_{\omega,s}\hat{a}^\dagger_{\omega',s}] = \mathrm{sgn}(\omega)\delta(\omega-\omega')$. The joint spectral amplitude,

$$S(\Omega,\omega) = [\alpha_{\mathrm{p}} E_{\mathrm{p}}(\Omega-\omega) + \alpha^*_{\mathrm{p}} E^*_{\mathrm{p}}(\omega-\Omega)]\zeta_{\Omega,\omega}, \quad (3)$$

is determined by two components. First, by the phase-matching function,

$$\zeta_{\Omega,\omega} = -\mathrm{i}d\,\mathrm{sgn}(\omega\Omega)\sqrt{\frac{|\omega\Omega|}{n_\Omega n_\omega}}\frac{L}{2c}\mathrm{sinc}(\eta_{\omega,\Omega}), \quad (4)$$

$$\eta_{\Omega,\omega} = \frac{L}{2c}[\omega(n_\omega - n_{\omega-\Omega}) - \Omega(n_\Omega - n_{\Omega-\omega})], \quad (5)$$

including the speed of light c. Second, by the coherent z-polarized ultrabroadband NIR probe of amplitude α_{p}, beam-waist area $A = \pi(3\ \mu\mathrm{m})^2$, and spectrum

$$E_{\mathrm{p}}(\omega) = \mathrm{i}\left(\frac{\hbar}{4\pi c\varepsilon_0 A}\right)^{1/2}\sqrt{\frac{|\omega|}{n_\omega}}f_{\mathrm{p}}(\omega), \quad (6)$$

with the vacuum permittivity ε_0 and the reduced Planck constant $\hbar$. The mode function $f_{\mathrm{p}}(\omega)$ of the probe is assumed to be Gaussian,

$$f_{\mathrm{p}}(\omega) = \kappa_{\mathrm{p}}\exp[-(\omega-\omega_{\mathrm{p}})^2/(2\sigma_{\mathrm{p}})^2 - \mathrm{i}t_{\mathrm{p}}\omega], \quad (7)$$

$$\kappa_{\mathrm{p}} = \left\{\sqrt{\frac{\pi}{2}}\sigma_{\mathrm{p}}\left[\mathrm{erfc}\left(\frac{-\omega_{\mathrm{p}}}{\sqrt{2}\sigma_{\mathrm{p}}}\right) - \mathrm{erfc}\left(\frac{\omega_{\mathrm{p}}}{\sqrt{2}\sigma_{\mathrm{p}}}\right)\right]\right\}^{-1/2}, \quad (8)$$

of bandwidth σ_{p} and central frequency ω_{p}. The normalization constant κ_{p} ensures that $\int_{-\infty}^{\infty}\mathrm{sgn}(\omega)|f_{\mathrm{p}}(\omega)|^2\mathrm{d}\omega = 1$.

The strength $S(\Omega,\omega)$ of the nonlinear interaction defined in Eq. (3) and thus the strength of the measurement is determined by a variety of factors. The photon number of the probe $N_{\mathrm{p}} = |\alpha_{\mathrm{p}}|^2$ in Eq. (3) is the most accessible parameter in an experiment and only affects the interaction or measurement strength. The latter statement also holds for the coupling constant d [see Eq. (4)]. However, the coupling constant is fixed by the choice of nonlinear crystal. The only other accessible physical quantity affecting the strength of the interaction is the sampled space-time volume $c\Delta t\Delta x\Delta y\Delta z$. The transversal area swept by the beam within the nonlinear crystal is that of the beam waist, $\Delta x\Delta y = A$, whose effect on the interaction strength can be seen through Eq. (6). The product of the longitudinal and temporal components of the space-time volume $c\Delta t\Delta z$ is the $(1+1)$-dimensional space-time area traced by the probe pulse traversing the nonlinear crystal. The quantity $c\Delta t\Delta z$ depends nontrivially on the combined effect of the pulse shape [Eq. (7)] and the phase matching [Eq. (4)], as shown in Ref. [46]. The variance of the zero-point fluctuations of the electromagnetic field depends inversely on the sampled space-time volume, a dependence also theoretically predicted for the variance of the electro-optic signal [46], and experimentally confirmed in Ref. [64]. Decreasing the beam-waist area leads to a decrease in the sampled space-time volume, which in turn enhances the strength of the interaction. For the application to quantum state tomography, the sampled space-time volume decides which part of the quantum state is reconstructed and therefore cannot be chosen arbitrarily.

A closer inspection of Eq. (3) lets us differentiate four frequency domains corresponding to different nonlinear processes. If both the high and the low frequencies are positive ($\omega > 0$ and $\Omega > 0$), the first summand in the right-hand side of Eq. (3) is exponentially suppressed due to $E_{\mathrm{p}}(\Omega-\omega)$ selecting Ω frequencies far beyond the MIR. Consequently, only $E^*_{\mathrm{p}}(\omega-\Omega)$ contributes, favoring frequencies obeying $|\omega| \sim \omega_{\mathrm{p}} + |\Omega|$. The detected s-polarized high-frequency excitations therefore correspond to sum-frequency generation. The conjugate process ($\omega < 0$ and $\Omega < 0$), on the other hand, suppresses the second summand in Eq. (3). SFG together with its conjugate process results in a beam-splitter-like contribution to Eq. (2). If the high and low frequency have opposite signs (i.e., $\omega > 0$ and $\Omega < 0$ or $\omega < 0$ and $\Omega > 0$), the detected high frequencies can be associated with difference-frequency generation and modes fulfilling $|\omega| \sim \omega_{\mathrm{p}} - |\Omega|$ are favored. Again, one of the summands on the right-hand side of Eq. (3) is exponentially suppressed. Considering DFG together with its conjugate process results in a squeezing-like contribution to Eq. (2) [73]. The transformation of the MIR spectrum under the two processes (SFG and DFG) is schematically shown in Fig. 2(b). For a detailed derivation of the nonlinear unitary operator, Eq. (2), see Ref. [54].

C. Filter and split stage

To allow for a more versatile description, we assume that the probe and local oscillator pulses can differ: After the NIR pulse propagates through the nonlinear crystal, a polarizing beam splitter can be used to remove the z-polarized probe and a new coherent local oscillator pulse with amplitude β can be introduced as a replacement. The combined s- and z-polarized NIR modes are then spectrally filtered, (SF) in Fig. 2, to give a narrow

quasimonochromatic profile centered at $\tilde{\omega}$ and of bandwidth $\Delta\omega$, defining the mode

$$\hat{\mathfrak{u}}_{\tilde{\omega},\lambda} = \int_{-\infty}^{\infty} \mathrm{rect}\left(\frac{\tilde{\omega}-\omega}{\Delta\omega}\right)\hat{a}_{\omega,\lambda}\mathrm{d}\omega \tag{9}$$

for the polarization direction $\lambda = s,\ z$. The rectangular function, $\mathrm{rect}(x)$, is equal to 1 for $|x| < 1/2$, equal to $1/2$ for $|x| = 1/2$, and 0 for $|x| > 1/2$. The filtering gives some control over the ratio between DFG and SFG contribution to the signal [cf. Fig. 2(b)]. If frequencies above the central frequency of the probe are detected, $\tilde{\omega} > \omega_{\mathrm{p}}$, mainly SFG contributes to the signal while for the opposite case, $\tilde{\omega} < \omega_{\mathrm{p}}$, DFG is dominant [45].

The filtered local oscillator together with the filtered s-polarized NIR excitations generated by the nonlinear interaction are split spectrally into multiple narrow-band pulses, as indicated in Fig. 2 (SP). This allows one to measure different quadratures of the MIR modes simultaneously using the different quasimonochomatic spectral splits. The spectral filtering together with the splitting of the modes can be achieved simultaneously by spectrally fanning out the pulses using a prism and selecting the respective quasimonochromatic frequency bands using an aperture, as depicted in Fig. 2(c). Alternatively, a bandpass filter could be used to select the quasimonochromatic band of width $\Delta\tilde{\omega}$ and a beam splitter to enable the simultaneous measurement on two quasimonochromatic NIR mdoes, as shown in Appendix A. We will follow the former implementation in the main text. The new pulses $i \in I = \{X, Y\}$ are characterized by a central frequency $\tilde{\omega}_i$ and a bandwidth $\Delta\tilde{\omega}_i$ and define a set of discrete modes $\hat{\mathfrak{u}}_{\tilde{\omega}_i,\lambda} = (\Delta\omega_i)^{-1/2}\int_{-\infty}^{\infty}\mathrm{rect}[(\tilde{\omega}_i-\omega)/\Delta\omega_i]\hat{a}_{\omega,\lambda}\mathrm{d}\omega$. To express the total NIR mode operator, $\hat{\mathfrak{u}}_{\tilde{\omega},\lambda} = \sum_{i\in I}\tilde{\alpha}_i\hat{\mathfrak{u}}_{\tilde{\omega}_i,\lambda}$, in terms of the set of discrete mode operators, we have to choose $\tilde{\alpha}_i = \sqrt{\Delta\omega_i/\Delta\omega}$ and require $\sum_{i\in I}\mathrm{rect}[(\tilde{\omega}_i-\omega)/\Delta\omega_i] = \mathrm{rect}[(\tilde{\omega}-\omega)/\Delta\omega]$. The latter condition ensures that both spectral cuts are correlated through the nonlinear interaction with practically the same MIR frequency range (and therefore the same nonmonochromatic mode). In case of two spectral cuts with equal bandwidth $\Delta\omega_X = \Delta\omega_Y = \Delta\omega/2$ and, therefore, $\tilde{\alpha}_X = \tilde{\alpha}_Y = 1/\sqrt{2}$, the total NIR operator is composed of two modes, $\hat{\mathfrak{u}}_{\tilde{\omega}_X,\lambda}$ and $\hat{\mathfrak{u}}_{\tilde{\omega}_Y,\lambda}$, one for detecting the X and one for the Y quadrature:

$$\hat{\mathfrak{u}}_{\tilde{\omega},\lambda} = \frac{1}{\sqrt{2}}(\hat{\mathfrak{u}}_{\tilde{\omega}_X,\lambda} + \hat{\mathfrak{u}}_{\tilde{\omega}_Y,\lambda}). \tag{10}$$

We will denote discretized mode operators, defined over a frequency range, with $\mathfrak{u}$, $\mathfrak{a}$, etc. This distinction is important because the usual discrete-mode commutation relations are violated by pairs of such operators defined over overlapping frequency bands. Therefore, we assume, throughout this work, that detected frequency bands are so selected that no such overlaps can happen.

The replacement of the probe by a local oscillator pulse together with the frequency splitting of the z-polarized modes can be described by the displacement operators $\hat{D}_{\tilde{\omega}_i,z}(\beta_i) = \exp(\beta_i\hat{\mathfrak{u}}^{\dagger}_{\tilde{\omega}_i,z} - \mathrm{H.c.})$ with amplitudes $\beta_i = \tilde{\alpha}_i\beta$, where β is the postfiltered local oscillator amplitude.

D. Ellipsometry stage

Subsequent to the filter and split stage, we assume that an ellipsometry on each NIR mode $\hat{\mathfrak{u}}_{\tilde{\omega}_i,\lambda}$ is performed: A ϕ_i-wave plate rotated by an angle θ_i, (WP) in Fig. 2, makes the signal at each ellipsometry stage balanced. We choose the signal to be balanced, i.e., to yield zero average signal for a MIR state for which all quadrature expectation values vanish, because noise affecting both polarizations the same way cancels out (see Ref. [66], Sec. III for details). The action of the wave plate is assumed to be independent of the frequency on each frequency band $\Delta\omega_i$ and can thus be modeled by $\hat{U}_{\tilde{\omega}_i,\mathrm{WP}} = \exp(\mathrm{i}\phi_i\hat{\mathfrak{u}}^{\dagger}_{\tilde{\omega}_i,\theta_i}\hat{\mathfrak{u}}_{\tilde{\omega}_i,\theta_i})$, where $\hat{\mathfrak{u}}_{\tilde{\omega}_i,\theta_i} = \cos(\theta_i)\hat{\mathfrak{u}}_{\tilde{\omega}_i,s} + \sin(\theta_i)\hat{\mathfrak{u}}_{\tilde{\omega}_i,z}$ is the bosonic operator acting on the mode with polarization parallel to the optical axis of the wave plate. The simultaneous measurement of two noncommuting quadratures, i.e., $\hat{X}$ and $\hat{Y}$, can be achieved by using a half-wave plate ($\varphi_X = \pi$) rotated by $\theta_X = 22.5°$ for the $\hat{X}$ quadrature and a quarter-wave plate [$\varphi_Y = (\pi/2)$] rotated by $\theta_Y = 45°$ for the electric field related $\hat{Y}$ quadrature. The action of the HWP and QWP on the z-polarized local oscillator and the s-polarized NIR excitations is depicted schematically in Figs. 2(d)–2(g) and Figs. 2(h)–2(k). Both wave plates mix the s- and z-polarized modes of the NIR field, enabling the interference of the local oscillator with the nonlinearly generated NIR excitations. However, the HWP introduces a relative phase between the local oscillator and the NIR excitations of π in the s polarization, while the QWP adds a relative phase of $+(\pi/2)$ $[-(\pi/2)]$ to the z polarization (s polarization). Thus, the HWP and QWP lead to orthogonal quadrature measurements. The total time evolution of the combined polarization NIR system is described by

$$\hat{U} = \hat{U}_{\mathrm{WP}}\hat{D}_{\tilde{\omega}}(\vec{\beta})\hat{U}_{\mathrm{NL}}, \tag{11}$$

with $\hat{U}_{\mathrm{WP}} = \otimes_i \hat{U}_{\tilde{\omega}_i,\mathrm{WP}}$ and $\hat{D}_{\tilde{\omega}}(\vec{\beta}) = \otimes_i \hat{D}_{\tilde{\omega}_i,z}(\beta_i)$. After the wave plate, the s- and z-polarized photons are spatially separated with the aid of polarizing beam splitters, (PBS) in Fig. 2. The photon number in each polarization of every frequency cut $\tilde{\omega}_i$ is measured using photon detectors, (D) in Fig. 2. The electro-optic signals are the photon-count differences described by

$$\Delta\hat{n}_i = \int_{-\infty}^{\infty}\mathrm{rect}\left(\frac{\tilde{\omega}_i-\omega}{\Delta\omega_i}\right)(\hat{n}_{\omega,s} - \hat{n}_{\omega_i,z})\mathrm{d}\omega. \tag{12}$$

By exploiting the narrow bandwidth of the operators $\hat{\mathbf{u}}_{\tilde{\omega}_i,\lambda}$, we can approximate the photon number,

$$\hat{\mathbf{n}}_{\tilde{\omega}_i,\lambda} = \int_{-\infty}^{\infty} \mathrm{rect}\left(\frac{\tilde{\omega}_i - \omega}{\Delta\omega}\right) \hat{a}^{\dagger}_{\omega,\lambda}\hat{a}_{\omega,\lambda}\mathrm{d}\omega \approx \hat{\mathbf{u}}^{\dagger}_{\tilde{\omega}_i,\lambda}\hat{\mathbf{u}}_{\tilde{\omega}_i,\lambda}, \quad (13)$$

and thus express the photon-number difference in terms of the photon number in each (polarization) mode with frequency $\tilde{\omega}_i$,

$$\Delta\hat{n}_i \approx \hat{\mathbf{n}}_{\tilde{\omega}_i,s} - \hat{\mathbf{n}}_{\tilde{\omega}_i,z} = \sum_{\Delta n_i=-\infty}^{\infty} \Delta n_i \hat{P}_{\Delta n_i}. \quad (14)$$

In the last step of the above equation, we decomposed the observable $\Delta\hat{n}_i$ into projectors,

$$\hat{P}_{\Delta n_i} = \sum_{n_i=\tilde{n}_i}^{\infty} |n_i + \Delta n_i\rangle_{i,s\,i,s}\langle n_i + \Delta n_i| \otimes |n_i\rangle_{i,z\,i,z}\langle n_i|, \quad (15)$$

onto the eigenspace of NIR Fock states with a photon-number difference Δn_i between the s- and z-polarized component. The summation starts at $\tilde{n}_i = \max\{0, -\Delta n_i\}$ to avoid negative photon-number counting.

The projection operator in Eq. (15), as well as the total time-evolution operator in Eq. (11), with the exception of the nonlinear unitary $\hat{U}_{\mathrm{NL}}$, are equivalent to the corresponding operators used in Ref. [66]. While the unitary defined by Eq. (2) describes a squeezing interaction between a continuum of modes, the unitary operator,

$$\hat{U}_{\mathrm{NL,MONO}} = \exp\left(\zeta^* \hat{a}_{\Omega,s} \sum_{i\in I} \tilde{\alpha}_i \hat{a}_{i,s} - \mathrm{H.c.}\right), \quad (16)$$

used in Ref. [66], describes a squeezing interaction between a monochromatic MIR mode $\hat{a}_{\Omega,s}$ and a nonmonochromatic NIR mode $\sum_{i\in I}\tilde{\alpha}_i\hat{a}_{i,s}$ with the squeezing strength ζ. In the following, we will discuss the conversion of Eq. (2) into such an effective two-mode operator.

E. First-order unitary

In principle, it is possible to write the nonlinear unitary operator in Eq. (2) in terms of discrete mode operators using a Schmidt decomposition [74,75]. Thus, the time evolution in the nonlinear crystal can be understood as only acting on a countably infinite number of effective nonmonochromatic modes instead of a continuum of modes. However, a Schmidt decomposition is in general computationally exhausting and selecting a set of most significant modes participating in the interaction can be a challenging task. Instead, the first-order unitary $\hat{U}^{[1]} = \exp(\hat{S}^{[1]})$, with

$$\hat{S}^{[1]} = \theta^{(1)}_{\tilde{\omega}}(\bar{\mathfrak{a}}_{\tilde{\omega}}\hat{\mathbf{u}}^{\dagger}_{\tilde{\omega}} - \mathrm{H.c.}), \quad (17)$$

can be used in place of Eq. (2), as shown in Ref. [54]. We will drop the index indicating the polarization from here on, since all operators in Eq. (17) act on the s-polarized modes. The broadband mode operator,

$$\bar{\mathfrak{a}}_{\tilde{\omega}} = \frac{1}{\theta^{(1)}_{\tilde{\omega}}}[\hat{\mathbf{u}}_{\tilde{\omega}}, \hat{S}] = \int_{-\Lambda}^{\Lambda} f_{\tilde{\omega}}(\Omega) e^{-\mathrm{i}t_{\mathrm{p}}\Omega}\hat{a}_{\Omega}\mathrm{d}\Omega, \quad (18)$$

with the mode function $f_{\tilde{\omega}}(\Omega) = (\theta^{(1)}_{\tilde{\omega}}\sqrt{\Delta\omega})^{-1} \times \int_{-\infty}^{\infty}\mathrm{rect}[(\tilde{\omega}-\omega)/\Delta\omega]S(\Omega,\omega)\mathrm{d}\omega$, normalized by the squeezing parameter $\theta^{(1)}_{\tilde{\omega}} = |[[\hat{S}, \hat{\mathbf{u}}^{\dagger}_{\tilde{\omega}}], [\hat{\mathbf{u}}_{\tilde{\omega}}, \hat{S}]]|^{1/2} \neq 0$, is not a pure annihilation or creation operator, since

$$[\bar{\mathfrak{a}}_{\tilde{\omega}}, \bar{\mathfrak{a}}^{\dagger}_{\tilde{\omega}}] = \int_{-\Lambda}^{\Lambda} \mathrm{sgn}(\Omega)|f_{\tilde{\omega}}(\Omega)|^2\mathrm{d}\Omega = \pm 1. \quad (19)$$

For $\int_0^{\Lambda}|f_{\tilde{\omega}}(\Omega)|^2\mathrm{d}\Omega > \int_{-\Lambda}^{0}|f_{\tilde{\omega}}(\Omega)|^2\mathrm{d}\Omega$ we will denote $\bar{\mathfrak{a}}_{\tilde{\omega}} = \hat{\mathfrak{a}}_{\tilde{\omega}}$ as an annihilation operator and for $\int_0^{\Lambda}|f_{\tilde{\omega}}(\Omega)|^2\mathrm{d}\Omega < \int_{-\Lambda}^{0}|f_{\tilde{\omega}}(\Omega)|^2\mathrm{d}\Omega$ as a creation operator $\bar{\mathfrak{a}}_{\tilde{\omega}} = \hat{\mathfrak{a}}^{\dagger}_{\tilde{\omega}}$. In either case, this operator is, in general, different from the ordinary annihilation or creation operator, because $\bar{\mathfrak{a}}_{\tilde{\omega}}|0\rangle \neq 0$ and $\langle 0|\bar{\mathfrak{a}}_{\tilde{\omega}} \neq 0$. Only if $\int_{-\Lambda}^{0}|f_{\tilde{\omega}}(\Omega)|^2\mathrm{d}\Omega = 0$ or $\int_0^{\Lambda}|f_{\tilde{\omega}}(\Omega)|^2\mathrm{d}\Omega = 0$, the operator $\bar{\mathfrak{a}}_{\tilde{\omega}}$ is actually an annihilation or creation operator of the (nonmonochromatic) Fock states.

Because the filtered bandwidth $\Delta\omega$ is assumed to be narrow, the mode function can be approximated by

$$f_{\tilde{\omega}}(\Omega) \approx \frac{\sqrt{\Delta\omega}}{\theta^{(1)}_{\tilde{\omega}}} S(\Omega,\tilde{\omega})e^{\mathrm{i}t_{\mathrm{p}}\Omega}, \quad (20)$$

$$\theta^{(1)}_{\tilde{\omega}} \approx \sqrt{\Delta\tilde{\omega}}\left|\int_{-\Lambda}^{\Lambda}\mathrm{sgn}(\Omega)|S(\Omega,\tilde{\omega})|^2\mathrm{d}\Omega\right|^{1/2}. \quad (21)$$

The spectrum of the MIR mode defined by Eq. (18) is thus determined by the joint spectral amplitude $S(\Omega,\tilde{\omega})$ with one of the frequencies fixed at the central frequency $\tilde{\omega}$ of the local oscillator, the detected frequency. Consequently, the squeezing parameter $\theta^{(1)}_{\tilde{\omega}}$ inherits the dependencies of $S(\Omega,\tilde{\omega})$ as discussed in Sec. II B. In particular, the squeezing parameter scales with the sampled (space-time) volume as $\theta^{(1)}_{\tilde{\omega}} \propto 1/\sqrt{\Delta x\Delta y\Delta z c\Delta t}$ [46,64]. An example of the joint spectral amplitude for a fixed $\tilde{\omega}$ can be seen in Fig. 3. The detected up-conversion processes at $\Omega \sim \tilde{\omega} - \omega_{\mathrm{p}}$ dominate the spectrum, since the down-conversion processes at $\Omega \sim \tilde{\omega} + \omega_{\mathrm{p}}$ are suppressed by phase matching. The up-conversion can be separated into the detected DFG, $\tilde{\omega} = \omega_{\mathrm{p}} - |\Omega|$ for $\Omega < 0$, and SFG, $\tilde{\omega} = \omega_{\mathrm{p}} + |\Omega|$ for $\Omega > 0$. If the central frequency ω_{p} of the probe is higher than the central frequency of the local oscillator, $\tilde{\omega} < \omega_{\mathrm{p}}$, DFG corresponding to the squeezing contributions in Eq. (17) prevails and we can write $\bar{\mathfrak{a}}_{\tilde{\omega}} = \hat{\mathfrak{a}}^{\dagger}_{\tilde{\omega}}$.

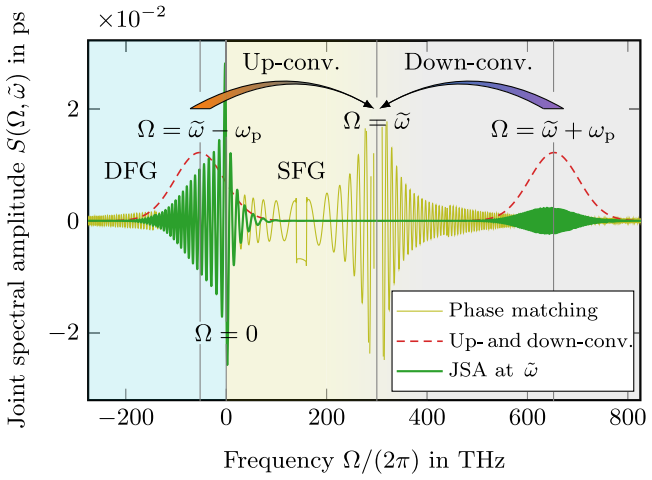

FIG. 3. Joint spectral amplitude (JSA) $S(\Omega,\tilde{\omega})$ at the detected local oscillator central frequency $\tilde{\omega}$, defining the mode function of $\bar{\mathbf{a}}_{\tilde{\omega}}$ [cf. Eq. (20)], as well as its two composing functions, the phase-matching function (solid light green line) $\zeta_{\Omega,\tilde{\omega}}$ and $\alpha_p E_p(\tilde{\omega}-\Omega)+\alpha_p{}^* E_p{}^*(\Omega-\tilde{\omega})$ describing the up- and down-conversion of the s-polarized photons of frequency Ω (dashed red line). The negative frequencies $\Omega<0$ of the up-conversion process correspond to the detected difference-frequency generation, $\tilde{\omega}=\omega_p-|\Omega|$, while the positive frequencies $\Omega>0$ correspond to sum-frequency generation, $\tilde{\omega}=\omega_p+|\Omega|$. We assumed $\tilde{\omega}=300$ THz, $\Delta\tilde{\omega}=1$ THz, $\omega_p=350$ THz, $\sigma_p=35$ THz, and $L=100$ μm. The model for the refractive index is given in Eq. (C1). The phase-matching function has two maxima, one at $\Omega=0$ and one at $\Omega=\tilde{\omega}$, while the probe contribution has maxima at $\Omega=\tilde{\omega}-\omega_p$ and $\Omega=\tilde{\omega}+\omega_p$, indicated by the vertical lines.

From now on, we focus on the case $\bar{\mathbf{a}}_{\tilde{\omega}}=\hat{\mathbf{a}}^\dagger_{\tilde{\omega}}$, which we will refer to as the squeezing regime. In this case, it is possible to decompose the operator as

$$\bar{\mathbf{a}}^\dagger_{\tilde{\omega}}=\hat{\mathbf{a}}_{\tilde{\omega}}=\cosh(\theta)\hat{\mathbf{a}}_{\mathrm{SA}}+\sinh(\theta)\sin(\theta_\perp)e^{-i\Phi_\perp}\hat{\mathbf{a}}^\dagger_{\mathrm{SA}}+\sinh(\theta)\cos(\theta_\perp)\hat{\mathbf{a}}^\dagger_{\mathrm{TH}},\tag{22}$$

with $\theta=\operatorname{arccosh}\left(\sqrt{\int_{-\Lambda}^{0}|f_{\tilde{\omega}}(\Omega)|^2 d\Omega}\right)$ and $\sin(\theta_\perp)e^{i\Phi_\perp}=\operatorname{csch}(\theta)\operatorname{sech}(\theta)\int_0^\Lambda f_{\tilde{\omega}}(\Omega)f_{\tilde{\omega}}(-\Omega)d\Omega$, as well as the two discretized (pure) annihilation operators $\hat{\mathbf{a}}_{\mathrm{SA/TH}}=\int_0^\Lambda f_{\mathrm{SA/TH}}(\Omega)e^{-it_p\Omega}\hat{a}_\Omega d\Omega$, with

$$f_{\mathrm{SA}}(\Omega)=\operatorname{sech}(\theta)f^*_{\tilde{\omega}}(-\Omega),\tag{23}$$

$$f_{\mathrm{TH}}(\Omega)=\sec(\theta_\perp)\operatorname{csch}(\theta)f_{\tilde{\omega}}(\Omega)-\tan(\theta_\perp)e^{i\Phi_\perp}f_{\mathrm{SA}}(\Omega).\tag{24}$$

As will become clear later, the DFG contribution and thus the operator $\hat{\mathbf{a}}_{\mathrm{SA}}$ corresponds to the part of the MIR spectrum sampled by the electro-optic sampling setup in Fig. 2, while $\hat{\mathbf{a}}_{\mathrm{TH}}$ represents the thermalized modes, which are unsampled but entangled through the nonlinear interaction to the sampled modes. By tracing over the entangled modes, the state of the sampled modes becomes partially mixed, resulting in an increased von Neumann entropy. Thus, the mode annihilated by $\hat{\mathbf{a}}_{\mathrm{TH}}$ thermalizes the state of the sampled modes [54]. The two operators commute by construction $[\hat{\mathbf{a}}_{\mathrm{SA}},\hat{\mathbf{a}}^\dagger_{\mathrm{TH}}]=0$, and because of the way the operators are constructed, the thermalized mode depends on the sampled mode; see Eq. (23). If the phase difference between the sampled mode and the modes contributing to the SFG is a multiple of π, $\Phi_\perp=n\pi$, the sampled frequencies attenuate the thermalized mode, as will become relevant in Sec. IV. The decomposition in Eq. (22) can be expressed using a unitary single-mode squeezing operator $\hat{S}\hat{\mathbf{a}}_{\mathrm{SA}}\hat{S}^\dagger=\mu_S\hat{\mathbf{a}}_{\mathrm{SA}}+\nu_S\hat{\mathbf{a}}^\dagger_{\mathrm{SA}}$ and two-mode squeezing operator $\hat{T}\hat{\mathbf{a}}_{\mathrm{SA}}\hat{T}^\dagger=\mu_T\hat{\mathbf{a}}_{\mathrm{SA}}+\nu_T\hat{\mathbf{a}}^\dagger_{\mathrm{TH}}$, with $\mu_{S/T}=\cosh(|\zeta_{S/T}|)$, $\nu_{S/T}=\exp[i\arg(\zeta_{S/T})]\sinh(|\zeta_{S/T}|)$. In order to write

$$\hat{\mathbf{a}}_{\tilde{\omega}}=\hat{S}\hat{T}\,\hat{\mathbf{a}}_{\mathrm{SA}}\hat{T}^\dagger\hat{S}^\dagger,\tag{25}$$

we have to choose

$$\zeta_S=e^{i\Phi_\perp}\operatorname{arccosh}\left\{[1-\tanh^2(\theta)\sin^2(\theta_\perp)]^{-1/2}\right\},\tag{26}$$

$$\zeta_T=\operatorname{arccosh}\left\{[\cosh^2(\theta)-\sinh^2(\theta)\sin^2(\theta_\perp)]^{1/2}\right\}.\tag{27}$$

The squeezing parameters $\theta^{(1)}_{\tilde{\omega}}$, $|\zeta_S|$, and ζ_T are numerically evaluated as a function of the up-converted frequency $\tilde{\omega}-\omega_p$ and the down-converted frequency $\tilde{\omega}+\omega_p$, in Fig. 4. If the maximum of the probe shape corresponding to the up-conversion process $\tilde{\omega}-\omega_p$ is shifted toward the origin or if the bandwidth of the probe σ_p is increased, the single- and two-mode squeezing parameters increase, since more SFG is involved in the nonlinear interaction, agreeing with the intuitive picture developed in Fig. 3.

Inserting Eq. (25) in the first-order unitary defined by Eq. (17) results in

$$\hat{U}^{[1]}=\hat{S}\hat{T}\,\hat{U}'_{\mathrm{NL}}\hat{T}^\dagger\hat{S}^\dagger,\tag{28}$$

with the effective two-mode squeezing operator

$$\hat{U}'_{\mathrm{NL}}=\exp\left[-\theta^{(1)}_{\tilde{\omega}}\left(\hat{\mathbf{a}}_{\mathrm{SA}}\sum_{i\in I}\tilde{\alpha}_i\hat{\mathbf{u}}_{\tilde{\omega}_i}-\mathrm{H.c.}\right)\right],\tag{29}$$

similar to the operator in Eq. (31), used in Ref. [66]. Utilizing the unitary transformation of the quadratic unitary operator in Eq. (28), the total time evolution can be expressed as

$$\hat{U}\approx\hat{S}\hat{T}\,\hat{U}_{\mathrm{eff}}\hat{T}^\dagger\hat{S}^\dagger,\tag{30}$$

where

$$\hat{U}_{\mathrm{eff}}=\hat{U}_{\mathrm{WP}}\hat{D}_{\tilde{\omega}}(\vec{\beta})\hat{U}'_{\mathrm{NL}}\tag{31}$$

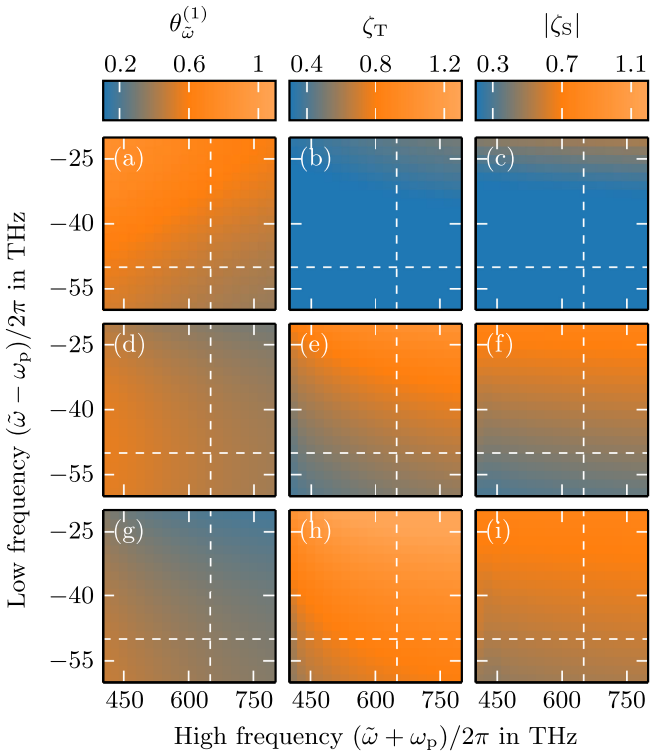

FIG. 4. The three squeezing parameters determining the nonlinear unitary defined in Eq. (28) as a function of the up-converted frequency $\tilde{\omega}-\omega_p$ and the down-converted frequency $\tilde{\omega}+\omega_p$ (cf. Fig. 3). Note that $\tilde{\omega}$ and ω_p are both considered variables. The nonlinear crystal is of length $L = 100$ μm and the refractive index given in Eq. (C1). The filtered local oscillator pulse bandwidth is chosen as $\Delta\tilde{\omega}/(2\pi) = 1$ THz. The probe pulse has the amplitude $\alpha_p = 2\times10^6$ and bandwidth is $\sigma_p/(2\pi) = 15$ THz for (a)–(c), $\sigma_p/(2\pi) = 35$ THz for (d)–(f), and $\sigma_p/(2\pi) = 50$ THz for (g)–(i). The white dashed lines indicate the point with $(\tilde{\omega}-\omega_p)/(2\pi) = -50$ THz and $(\tilde{\omega}+\omega_p)/(2\pi) = 650$ THz, which are the values used in our example for time-domain quantum state tomography in Sec. IV.

is the total, transformed time-evolution operator. The unitary operator $\hat{U}_{\text{eff}}$ is mathematically equivalent to the time evolution used in Ref. [66] and thus, by transforming the MIR state using the squeezing operators $\hat{S}$ and $\hat{T}$, one can apply the results from Ref. [66], as will be done in the following section.

III. DIFFERENCE-COUNT PROBABILITY DISTRIBUTION

The s-quasiprobability distributions $\rho(z;s)$ parametrized by a single (real) number s are a representation of a (possibly mixed) quantum state equivalent to the density operator $\hat{\rho}$, in the sense that all observable quantities calculated from either agree. The two representations can be related to one another via the s-characteristic function $\chi(\beta;s) = \exp(s|\beta|^2/2)\text{tr}[\hat{D}(\beta)\hat{\rho}]$, which is the Fourier transform of the s-quasiprobability distribution $\rho(z;s) = \pi^{-1}\int\exp(-2i\text{Im}[\beta z^*])\chi(\beta;s)d^2\beta$. For $s=-1$, 0, 1, the characteristic function corresponds to the expectation value of the antinormally, symmetrically, and normally ordered displacement operator and the respective s-quasiprobability distributions are the Husimi, Wigner, and Glauber-Sudarshan distributions [76–78]. For the electro-optic sampling of a single monochromatic mode, we have recently shown that the probability distribution of the measured photon-number difference is related to an s-quasiprobability distribution of the sampled quantum state [66]. In the case of electro-optic sampling with an ultrabroadband probe using the setup described in the previous section, the probability to measure the photon-number differences $\{\Delta n_i\}$ given the MIR modes, centered at $\tilde{\Omega}$, are in the initial broadband state $\hat{\rho}_{\tilde{\Omega}}$ reads

$$p(\{\Delta n_i\}) = \text{tr}\left(\hat{P}_{\{\Delta n_i\}}\hat{U}\hat{\rho}_{\tilde{\Omega}}\otimes|0\rangle_{\text{NIR NIR}}\langle 0|\hat{U}^\dagger\right). \quad (32)$$

We assume that the (ultrabroadband) NIR modes (after the removal of the z-polarized probe) are in the ground state $|0\rangle_{\text{NIR}}$ and the combined state of MIR and NIR modes is evolved using the unitary time-evolution operator $\hat{U}$ from Eq. (30) until a projective measurement, described by the projectors $\hat{P}_{\{\Delta n_i\}}$ defined in Eq. (15), is performed. Inserting Eq. (30) into Eq. (32) yields

$$p(\{\Delta n_i\}) \approx \text{tr}\Big[\hat{P}_{\{\Delta n_i\}}\hat{S}\,\hat{T}\,\hat{U}_{\text{eff}}\hat{T}^\dagger\hat{S}^\dagger\hat{\rho}_{\tilde{\Omega}} \otimes|0\rangle_{\text{NIR NIR}}\langle 0|\hat{S}\,\hat{T}\,\hat{U}^\dagger_{\text{eff}}\hat{T}^\dagger\hat{S}^\dagger\Big]. \quad (33)$$

The projectors $\hat{P}_{\{\Delta n_i\}}$ defined in Eq. (15) and the squeezing operators $\hat{S}$, $\hat{T}$ act on different frequency bands, and therefore, they commute. Thus, by defining a transformed and reduced density operator (in which tr_r is the trace over the modes not involved in the nonlinear interaction),

$$\hat{\tilde{\rho}}_{\text{SA}} = \text{tr}_r\left[\hat{T}^\dagger\hat{S}^\dagger\hat{\rho}_{\tilde{\Omega}}\hat{S}\,\hat{T}\right], \quad (34)$$

solely of the sampled modes, we can recast the count-probability distribution into

$$p(\{\Delta n_i\}) \approx \text{tr}_{\text{NIR}}\left\{\text{tr}_{\text{SA}}\left[\hat{P}_{\{\Delta n_i\}}\hat{U}_{\text{eff}}\hat{\tilde{\rho}}_{\text{SA}}\otimes|0\rangle_{\text{NIR NIR}}\langle 0|\hat{U}^\dagger_{\text{eff}}\right]\right\}. \quad (35)$$

Equation (35) involves only the (nonmonochromatic) sampled MIR mode and the NIR modes and allows one to apply the formalism developed in Ref. [66]. Thus, we can relate the count-probability distribution to the $\tilde{s}$-quasiprobability

distribution $\tilde{\rho}_{\mathrm{SA}}(z;s)$ of the transformed state in Eq. (34) through

$$p(\{\Delta n_i\}) \approx N\tilde{\rho}_{\mathrm{SA}}(z[\{\Delta n_i\}];\tilde{s}). \tag{36}$$

The quasiprobability distribution with parameter $\tilde{s} = 1\text{–}2\coth^2(|\theta^{(1)}_{\tilde{\omega}}|)$ depending on the squeezing parameter $\theta^{(1)}_{\tilde{\omega}}$ of the nonlinear interaction [cf. Eq. (17)] is renormalized by $N = \mathrm{csch}^2(|\theta^{(1)}_{\tilde{\omega}}|)/2$ and related to the discrete photon-count differences via its argument,

$$z(\{\Delta n_i\}) = \frac{1}{\sqrt{2}}\mathrm{csch}(|\zeta|)\left(\frac{\Delta n_X}{\beta_X} + \mathrm{i}\frac{\Delta n_Y}{\beta_Y}\right), \tag{37}$$

with amplitudes β_i of the postfiltered local oscillators. See Sec. II A for an intuitive explanation of this result. Equation (36) holds only for $|\tilde{\alpha}_X|^2 = |\tilde{\alpha}_Y|^2 = 1/2$. However, the result presented here can easily be generalized to measurements of multiple $\hat{X}$ and $\hat{Y}$ quadratures with different α_i by applying the full result of Ref. [66]. The simplified difference-count probability distribution suffices for our purpose. The nonmonochromatic s-quasiprobability distribution $\hat{\tilde{\rho}}_{\mathrm{SA}}$ of the transformed state can be related to the two-mode characteristic function $\chi_{\mathrm{TM}}(\beta_{\mathrm{SA}},\beta_{\mathrm{TH}}) = \mathrm{tr}[\hat{D}_{\mathrm{SA}}(\beta_{\mathrm{SA}})\hat{D}_{\mathrm{TH}}(\beta_{\mathrm{TH}})\hat{\rho}_{\tilde{\Omega}}]$, defined as the expectation value of the displacement operators acting on the modes SA and TH, by

$$\begin{aligned}\tilde{\rho}_{\mathrm{SA}}(z;s) &= \frac{1}{\pi}\int \chi_{\mathrm{SA}}(\beta;s)e^{-2i\,\mathrm{Im}(\beta z^*)}\mathrm{d}^2\beta \\ &= \frac{1}{\pi}\int \chi_{\mathrm{TM}}[\mu_{\mathrm{T}}(\mu_{\mathrm{S}}\beta - \nu_{\mathrm{S}}\beta^*), -\nu_{\mathrm{T}}\beta^*] \\ &\quad\times e^{-2i\,\mathrm{Im}(\beta z^*)+s|\beta|^2/2}\mathrm{d}^2\beta,\end{aligned} \tag{38}$$

as shown in Appendix A. The transformed s-quasiprobability distributions for broadband coherent states, cat states, and the squeezed vacuum can be taken from Appendix B.

If the broadband MIR mode is in some arbitrary state $\hat{\rho}_{\tilde{\Omega}}(\hat{\mathbf{a}}_{\tilde{\Omega}})$ defined in terms of a single nonmonochromatic mode operator $\hat{\mathbf{a}}_{\tilde{\Omega}} = \int_0^\infty f_{\tilde{\Omega}}(\Omega)e^{-\mathrm{i}t_{\tilde{\Omega}}\Omega}\hat{a}_\Omega \mathrm{d}\Omega$, completely overlapping with the transversal mode of the probe, the two-mode characteristic function can be calculated using the decomposition

$$\hat{\mathbf{a}}_{\tilde{\Omega}} = A_{\mathrm{SA}}(\Delta t)\hat{\mathbf{a}}_{\mathrm{SA}} + A_{\mathrm{TH}}(\Delta t)\hat{\mathbf{a}}_{\mathrm{TH}} + A_{\mathrm{UN}}(\Delta t)\hat{\mathbf{a}}_{\mathrm{UN}}, \tag{39}$$

where the coefficients $A_x(\Delta t) = [\hat{\mathbf{a}}_{\tilde{\Omega}}, \hat{\mathbf{a}}_x^\dagger]$ ($x = \mathrm{SA}$, TH, UN) quantify the amount the sampled, thermalized, and unsampled mode contribute to the MIR mode. The newly introduced operator $\hat{\mathbf{a}}_{\mathrm{UN}}$ of the unsampled and uncorrelated modes, leaving the electro-optic signal unaffected, has to be differentiated from the thermalized mode, which is also unsampled, but correlated to the sampled mode, therefore altering the measurement. All operators on the right-hand side of Eq. (39) commute. The coefficients $A_x(\Delta t)$ can be expressed as the convolution of the Fourier-transformed mode functions $\mathcal{F}[f_{\tilde{\Omega}}](t)$ and the gating function $\mathcal{F}[f_x^*](t)$, dependent on the relative time delay $\Delta t = t_{\tilde{\Omega}} - t_{\mathrm{p}}$ between the sampled MIR pulse and the NIR probe pulse according to

$$A_x(\Delta t) \approx (\mathcal{F}[f_{\tilde{\Omega}}] * \mathcal{F}[f_x^*])(\Delta t). \tag{40}$$

Therefore, the coefficients can be understood as the waveform of the MIR pulse $\mathcal{F}(f_{\tilde{\Omega}})$ averaged over a time window defined by $\mathcal{F}(f_x)$.

The parameter $\tilde{s}$ of the broadband quasiprobability distribution has another significance, as becomes apparent from analyzing the variance of the difference counts Δn_i, as done in Appendix D. The variance in Eq. (D2) is composed of two contributions, one dependent on the MIR state and one dependent only on the parameter of the nonlinear interaction. Since the former contribution is more intricate, we will postpone its discussion to Sec. III B and focus on the latter contribution, which we will call measurement noise. The measurement noise is given by $\sqrt{-\tilde{s}/4}$ and thus depends only on the two-mode squeezing parameter $\theta^{(1)}_{\tilde{\omega}}$, which in turn depends on the photon number of the probe pulse $N_{\mathrm{p}} = |\alpha_{\mathrm{p}}|^2$. Figure 5

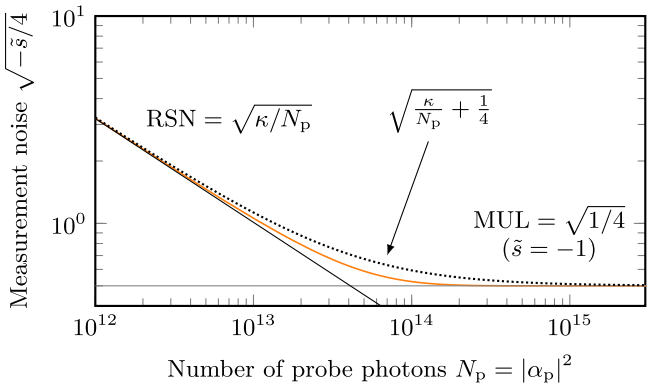

FIG. 5. Dependence of the measurement noise $\sqrt{-\tilde{s}/4}$, the state-independent part of the variance in Eq. (D2), on the photon number of the probe $N_{\mathrm{p}} = |\alpha_{\mathrm{p}}|^2$. In the low-photon-number limit, the measurement noise is dominated by the relative shot noise (RSN), the ratio between shot noise and probe photon number resulting in $\sqrt{\kappa/N_{\mathrm{p}}}$, with the proportionality constant κ depending on the $\theta^{(1)}_{\tilde{\omega}}$ [Eq. (21)] and thus primarily depends on the SFG and DFG contributions to the joint spectral amplitude $S(\tilde{\omega},\Omega)$ as shown in Figs. 4(a), 4(d), and 4(g). In the high-photon-number limit, the measurement noise approaches an asymptote given by measurement uncertainty limit (MUL) at $\sqrt{1/4}$. The Pythagorean addition of shot noise and MUL (dotted black line) overestimates the full result (solid orange line). The former is qualitatively equivalent to the result obtained by Moskalenko *et al.* [46].

shows the dependence of the measurement noise on the probe photon number N_p. For a small photon number, the measurement noise is dominated by the relative shot noise (RSN) $\sqrt{\kappa/N_p}$, i.e., the ratio between shot noise $\sqrt{N_p}$ and probe photon number N_p. The proportionality constant $\sqrt{\kappa}$ depends on the difference between DFG and SFG contributions to the joint spectral amplitude, Eq. (3). For large photon numbers, the measurement noise asymptotically approaches $1/2$. The bound is due to the measurement uncertainty limit (MUL) [67–69] and is fundamentally insurmountable, since the bound $\tilde{s} \leq -1$ ensures the nonnegativity of the difference-count probability distribution given in Eq. (36). The measurement noise is overestimated by the Pythagorean addition of shot noise and measurement uncertainty limit, as predicted by the perturbative theory in [46]. The first-order unitary enables a description of the nonlinear interaction beyond the perturbative approach, giving the theory of quantum electro-optic sampling developed in this work validity even in the high probe-photon-number regime. While the probe amplitude α_p can be related to the measurement noise, the local oscillator amplitude $|\beta|$ only rescales the probability distribution, since its sole effect is on the argument of the quasiprobabilty distribution in Eq. (37).

A. Homodyne limit

It is instructive to consider the following special case of the result in Eq. (36). First, we assume that the probe bandwidth is rather narrow with $\sigma_p/(2\pi) = 5$ THz such that only DFG contributes to the nonlinear interaction and

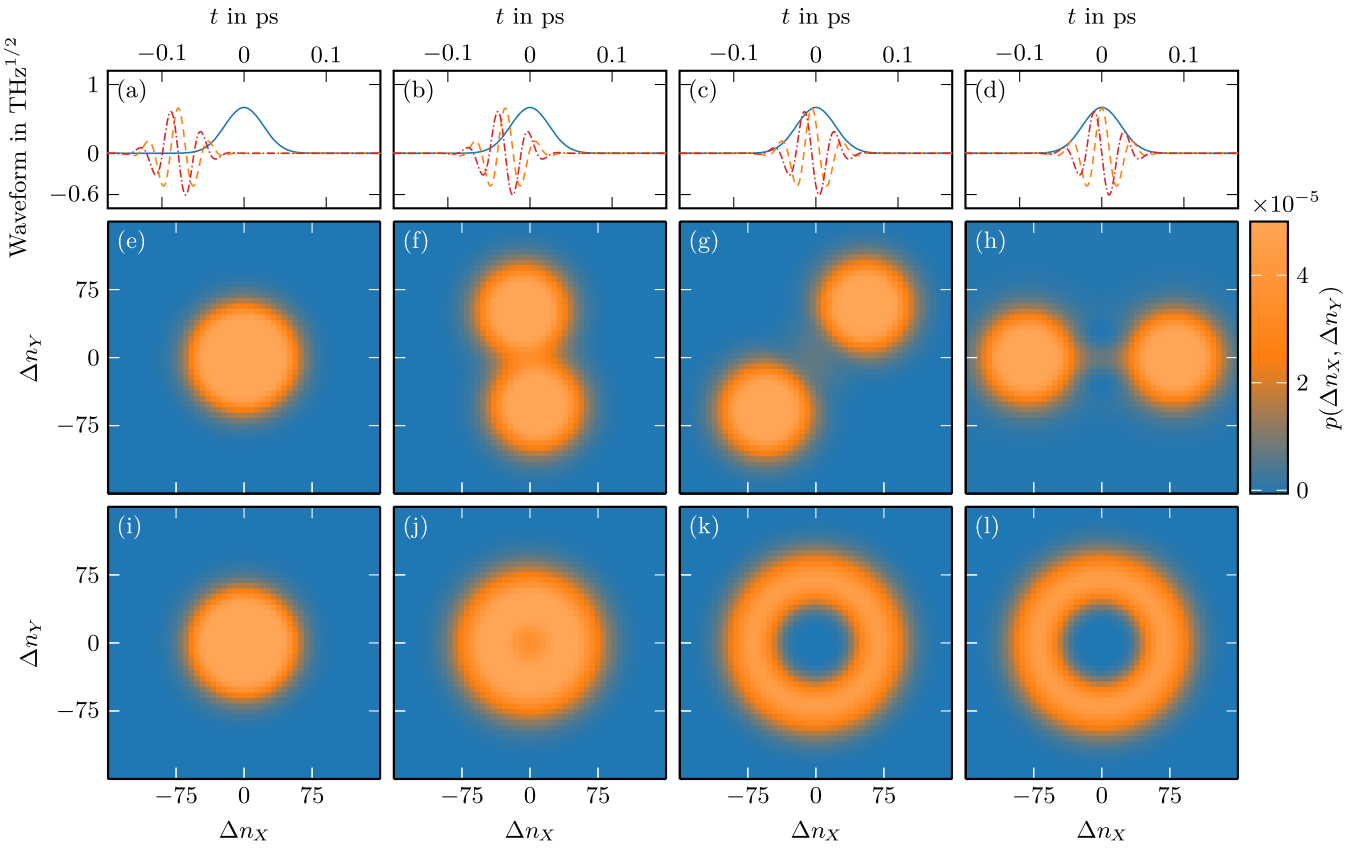

FIG. 6. (a)–(d) Envelope of the gating function $|\mathcal{F}[f_{SA}](t)|$ (solid blue line) and the waveform of the MIR $\mathcal{F}[f_{\tilde{\Omega}}](t)$ (dashed orange line for the real part and dash-dotted red line for the imaginary part) in the time domain. The time delay of the MIR $t_{\tilde{\Omega}} = -2\pi t_{step}/\tilde{\Omega}$ is varied in (a)–(d) by $t_{step} = 2, \frac{3}{4}, \frac{1}{8}, 0$. The probe pulse is a coherent state with a large amplitude $\alpha_p = 2 \times 10^7$ and of a Gaussian shape defined by Eq. (7) centered at $\omega_p/(2\pi) = 325$ THz and of bandwidth $\sigma_p/(2\pi) = 5$ THz with a fixed time delay $t_p = 0$ s, while the MIR is a Gaussian centered at $\tilde{\Omega}/(2\pi) = 25$ THz and of bandwidth $\sigma_{\tilde{\Omega}}/(2\pi) = 5$ THz. The filtered local oscillator pulse is of amplitude $\beta = \sqrt{2} \times 0.1$ and of bandwidth $\Delta\omega/(2\pi) = 1$ THz at $\tilde{\omega}/(2\pi) = 300$ THz. The local oscillator amplitude only scales the probability distribution, leading to a concentration around low photon-number difference in this case (see end of Sec. III for details). The crystal is assumed to be of length $L = 6$ μm and made of zinc telluride with the refractive index of Fig. 11. The waveform of the gating function and the sampled state are thus matched at zero relative time delay; see (d). Together with the strong probe amplitude, Eq. (38) relates the count-probability distributions over $\{\Delta n_X, \Delta n_Y\}$ the broadband Husimi function of the MIR state (see homodyne limit in Sec. III A), associating Δn_X with $\hat{X}$-quadrature and Δn_Y with $\hat{Y}$-quadrature measurements. (e)–(h) Example of the count-probability distribution in Eq. (36) for a cat state with $\alpha_{\tilde{\Omega}} = 2$, (i)–(l) for a Fock state with $n_{\tilde{\Omega}} = 3$.

the squeezing parameters $\zeta_S, \zeta_T \approx 0$ effectively vanish. Furthermore, we (rather unrealistically) assume a large probe amplitude, $|\alpha_p| = 2 \times 10^7$, resulting in $\tilde{s} \approx -1$ (see Fig. 5 for the parameter $\tilde{s}$ as function of the probe photon number $N_p = |\alpha_p|^2$). In this limit, the quasiprobability distribution in Eq. (36) approaches the Husimi function of the sampled MIR state. We call this the homodyne limit, since this reproduces the results one would obtain using homodyne detection. However, in contrast to conventional pulsed homodyne detection [1–9], where the waveform of the local oscillator and the sampled state are usually matched to optimize detection efficiency, in our approach the two can be time delayed against one another. If the waveform of the state averaged over the gating function is zero and thus $|A_{UN}(\Delta t)| = 1$, the transformed s-quasiprobability distribution describes the vacuum, corresponding to the scenario in Figs. 6(a), 6(e), and 6(i). The key idea to understand our approach to time-domain quantum state tomography is the following: As the relative time delay Δt is varied, the time window is shifted and different parts of the MIR waveform are averaged over. This can increase the contributions from the MIR state to the transformed quasiprobability distribution $\tilde{\rho}_{SA}(z; s)$ depending on the average waveform, thus dynamically sampling the MIR state as shown row by row in Fig. 6 for the MIR in a cat state with amplitude $\alpha_{\tilde{\Omega}} = 2$, Figs. 6(e)–6(h), and a Fock state with $n_{\tilde{\Omega}} = 3$, Figs. 6(i)–6(l).

The MIR quasiprobability distribution of the cat states can be decomposed into three parts (a proper definition is given in Sec. B 2),

$$\tilde{\rho}_{SA}(z; s|\text{cat}) \propto \rho_{SA}(z; s|\alpha_{\tilde{\Omega}}) + \rho_{SA}(z; s| - \alpha_{\tilde{\Omega}}) + \exp\left(-2|A_{UN}(\Delta t)\alpha_{\tilde{\Omega}}|^2\right)\rho_{osc}(z; s), \quad (41)$$

with the first two terms corresponding to a coherent state with amplitude $\pm\alpha(\Delta t)$ and the third term accounting for the oscillatory part due to the coherent superposition of the two coherent states. Compared to the quasiprobability distribution of a monochromatic cat state, the oscillatory part is exponentially suppressed by the coefficient of the unsampled mode $A_{UN}(\Delta t)$ defined through Eq. (39). Thus, to best reconstruct the oscillations, which are the hallmark for the quantum nature of the cat state, the waveform of the gating function $\mathcal{F}[f_{SA}](t)$ should be matched to the MIR waveform.

By defining $p_{\Delta t} = |A_{SA}(\Delta t)|^2$ and denoting the quasiprobability distribution of a k-photon Fock state with $\rho_k(z; s)$, we see that the sampled quasiprobability distribution of a n-photon Fock state,

$$\tilde{\rho}_{SA}(z; s|n) = \sum_{k=0}^{n} \binom{n}{k} p_{\Delta t}^k (1 - p_{\Delta t})^{n-k} \rho_k(z; s), \quad (42)$$

corresponds to a mixture of Fock states weighted by a binomial distribution. Since the probability of one photon being detected in the sampled waveform is $p_{\Delta t}$, the probability of detecting k out of n photons is binomially distributed [the coefficient $A_{TH}(\Delta t)$ for the thermalized mode is zero in the homodyne limit].

The narrow frequency band of the gating function in the homodyne limit requires a good matching to the frequency band of the sampled MIR state and thus some information about the spectrum of the MIR state has to be known in advance. In addition, the small bandwidth leads to an extended time window $\mathcal{F}(f_{SA})$ over which the MIR waveform is averaged. The time averaging in turn causes a deviation of the sampled quasiprobability distribution from the actual dynamics of the state, limiting the temporal resolution [visible in Fig. 6(f) since the axis of the cat state is not vertical as expected at 3/4 of the oscillation period]. Thus, to simultaneously sample the quasiprobability distribution of a quantum state along with its complete waveform, the probe pulse has to be ultrabroadband to cover a larger frequency band, and short in the time domain to reduce averaging of the waveform. However, this requires us to take the thermalized mode into our considerations.

B. Thermalization

As already mentioned in the previous section, the transformed quasiprobability distribution in Eq. (38) turns into the quasiprobability distribution of the sampled state $\hat{\rho}_{SA} = \text{tr}_r(\hat{\rho}_{\tilde{\Omega}})$, if only DFG contributes to the nonlinear interaction, i.e., $\zeta_S, \zeta_T = 0$. Increasing the SFG will add some contribution from the thermalized mode to the transformed state $\tilde{\rho}_{SA}$. If the MIR mode is in the vacuum state and if the bandwidth of the probe is assumed to be $\sigma_p/(2\pi) = 15$ THz, DFG predominates and the difference-count probability distribution follows the quasiprobability

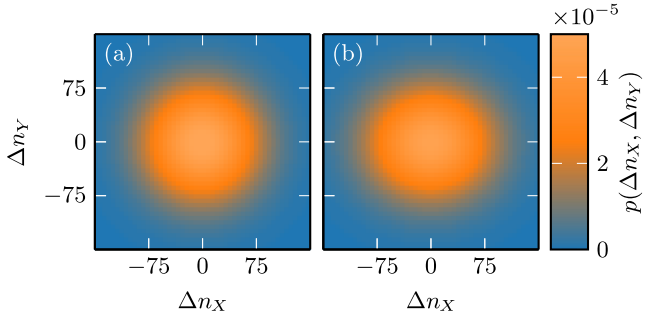

FIG. 7. Count-probability distribution [Eq. (36)] for a broadband MIR vacuum state with $\tilde{\Omega}/(2\pi) = 25$ THz, $\sigma_\Omega/(2\pi) = 5$ THz. For the filtered local oscillator, we assume $\tilde{\omega}/(2\pi) = 300$ THz, $\Delta\omega/(2\pi) = 1$ THz, and $\beta = 50$. We consider a crystal of length $L = 100$ μm. The parameters describing the probe are $\alpha_p = 2 \times 10^6$, $t_p = 0$ ps, $\omega_p/(2\pi) = 350$ THz. (a) The bandwidth of the probe is $\sigma_p/(2\pi) = 15$ THz and difference-frequency generation dominates the nonlinear interaction. (b) The probe bandwidth is $\sigma_p/(2\pi) = 50$ THz and the amount of sum-frequency generation to the nonlinear interaction is enhanced compared to the case in (a), resulting in some thermalization of the sampled quasiprobabilty distribution.

distribution of the vacuum, as can be seen in Fig. 7(a). However, if the bandwidth of the probe is assumed to be $\sigma_p/(2\pi) = 50$ THz, SFG contributes stronger to the nonlinear interaction and the difference-count probability distribution is squeezed due to the effect of the squeezing operators in Eq. (34) on the sampled state, visible in Fig. 7(b). It is again instructive to consider the variance of the photon-number difference in Eq. (D2). While the state-independent contribution was already discussed in Sec. III, the state-dependent contribution is more intricate. Since the latter can be expressed in terms of the variance of the transformed sampled MIR state, defined in Eq. (34), it includes contributions from the thermalized mode. For a coherent MIR input state $\hat{\rho}_{\tilde{\Omega}}$ (including the vacuum as a limit case), the main result from Ref. [54] in the squeezing regime can be reproduced and generalized. Equation (D9) shows that in the squeezing regime, i.e., $\bar{\mathfrak{a}}_{\tilde{\omega}} = \hat{\mathfrak{a}}^{\dagger}_{\tilde{\omega}}$, thermalization leads to an increase of the variance, which we will call thermalization noise from here on. The thermalization noise can be mitigated by filtering below the probe central frequency, $\tilde{\omega} \leq \omega_p$, as we discuss in the next section.

The influence of the thermalized mode on the dynamics of the sampled broadband squeezed MIR state can be seen in Fig. 8 and Eq. (B11). In addition to the time-dependent squeezing of the MIR state, the sampled quasiprobability distribution is squeezed and thermalized due to the nonlinear interaction in the nonlinear crystal. While the gating function of ultrabroadband electro-optic sampling has a

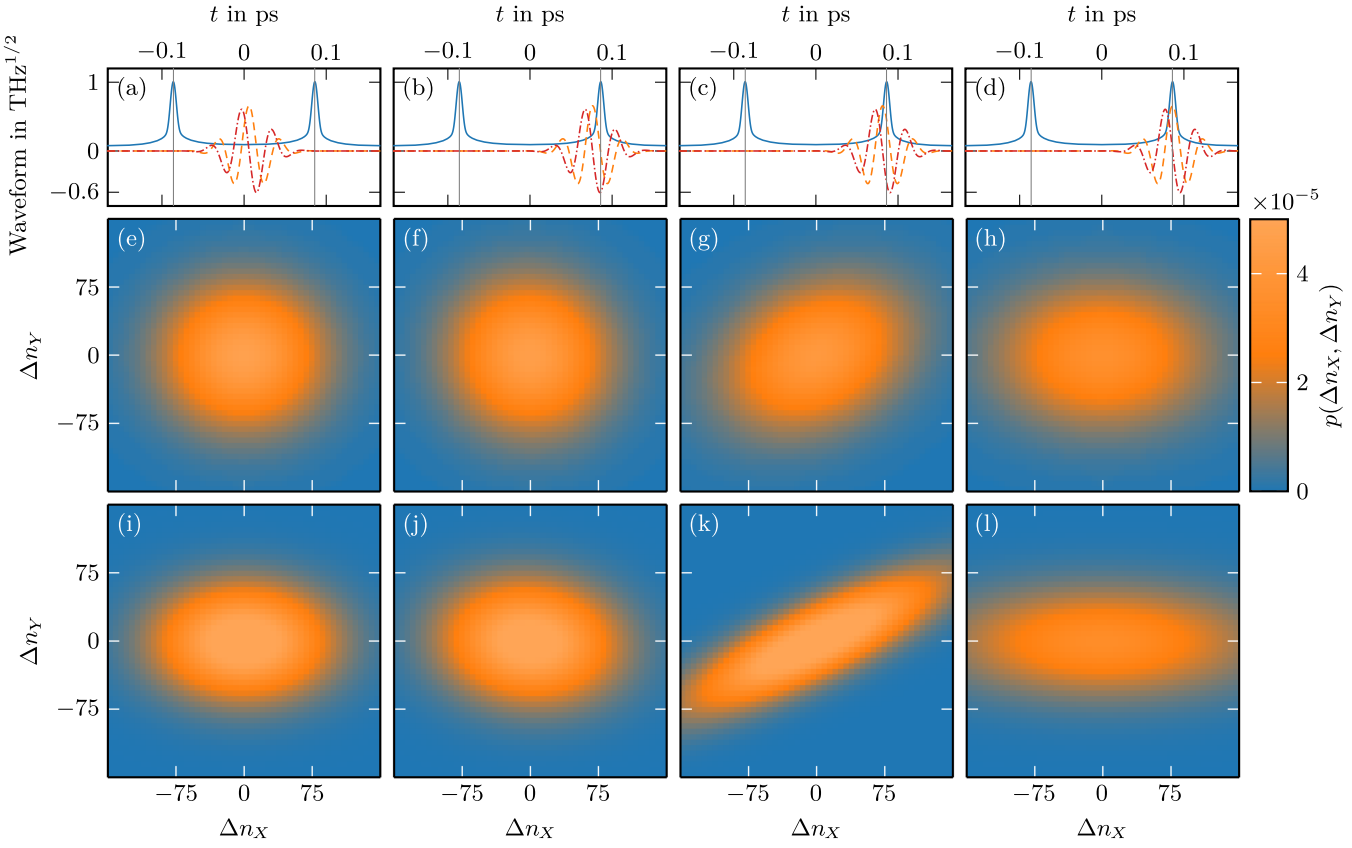

FIG. 8. (a)–(d) Envelope of the gating function $|\mathcal{F}[f_{SA}](t)|$ (solid blue line) with an ultrabroadband probe pulse compared to Fig. 6 and the temporal MIR waveform $\mathcal{F}[f_{\tilde{\Omega}}](t)$ (dashed orange line for the real part and dash-dotted red line for the imaginary part). The sampled mode has two maxima indicated by the vertical lines located one period $\eta_c = (L/2c)[n_g(\tilde{\omega}) - n(0)]$ of the (approximated) phase-matching function away from the origin (see Sec. IV, item 1). The time delay of the MIR $t_{\tilde{\Omega}} = \eta_c - 2\pi t_{step}/\tilde{\Omega}$ is varied in (a)–(d) by $t_{step} = 2, \frac{3}{4}, \frac{1}{8}, 0$. The probe pulse is of a Gaussian shape defined by Eq. (7) centered at $\omega_p/(2\pi) = 350$ THz and of bandwidth $\sigma_p/(2\pi) = 35$ THz with a fixed time delay $t_p = 0$ s, while the MIR is a Gaussian centered at $\tilde{\Omega}/(2\pi) = 25$ THz and of bandwidth $\sigma_{\tilde{\Omega}}/(2\pi) = 5$ THz. (e)–(l) Example of the count-probability distribution in Eq. (36) for a squeezed vacuum generated by the operator in Eq. (B7) with $\zeta_{\tilde{\Omega}} = 1.5$. (e)–(h) The coherent probe pulse has an amplitude of $\alpha_p = 2 \times 10^6$, while for (i)–(l) it is $\alpha_p = 2 \times 10^7$. Equation (38) shows the relation between the count-probability distributions over $\{\Delta n_X, \Delta n_Y\}$ and the quasiprobability distribution of the sampled quantum state, associating Δn_X with $\hat{X}$-quadrature and Δn_Y with $\hat{Y}$-quadrature measurements. The filtered local oscillator pulse is of amplitude $\beta = \sqrt{2} \times 10$ and of bandwidth $\Delta\omega/(2\pi) = 1$ THz at $\tilde{\omega}/(2\pi) = 300$ THz. The local oscillator amplitude only scales the probability distribution, leading to a concentration around low photon-number difference in this case (see end of Sec. III for details). The crystal is assumed to be of length $L = 100$ μm and made of zinc telluride with the refractive index of Fig. 11.

much better time resolution when compared to the homodyne limit [cf. Figs. 6(a)–(d) and 8(a)–8(d)], the sampled quasiprobability distribution is altered due to the nonlinear interaction. This is especially pronounced for a strong probe pulse with $\alpha_p = 2 \times 10^7$ [the large semiaxis of the squeezed distribution in Fig. 8(k) deviates from the diagonal, along which it would be expected for an eighth of a period of the MIR waveform]. This effect is less pronounced in the more realistic case of $\alpha_p = 2 \times 10^6$, shown in Figs. 8(e)–8(h). Thus, there seems to be a trade-off between the temporal resolution and the resolution in phase space. In Sec. IV we propose to circumvent this trade-off by making measurements with an ultrabroadband probe as well as measurements with the sampled mode matched to MIR mode to achieve a subcycle temporal resolution as well as the resolution in phase space required to resolve quantum states of light.

IV. SUBCYCLE TIME-DOMAIN QUANTUM STATE TOMOGRAPHY

A phase-sensitive measurement typically requires the comparison of the signal to a local oscillator. For pulse-based homodyne detection, the sampled pulsed modes and the local oscillator pulse are mixed in a beam splitter, while for electro-optic sampling they interact in a nonlinear crystal. The mixing unavoidably leads to an averaging of the detected modes over the duration (and oscillations) of the local oscillator pulse. The goal of optical time-domain quantum tomography is to reconstruct the quantum state of a system, namely the MIR state, such that the averaging is taken over a time interval below the duration of a single cycle of the MIR-pulse central frequency (i.e., subcycle), granting access to the dynamics of quantum systems. The reconstruction of the sampled MIR state and its dynamics using the quantum-electro-optic-sampling setup proposed in Sec. II is based on the relation between the photon-count probability distribution of the setup and the transformed $\tilde{s}$-quasiprobability distribution in Eq. (36). For each fixed relative time delay Δt between the NIR probe pulse and the sampled MIR pulsed mode, the transformed MIR $\tilde{s}$-quasiprobability distribution can be reconstructed from sampled data using the relation in Eq. (36). Performing the reconstruction for various relative time delays Δt gives access to the time dependence of the transformed MIR state and thus to the coefficients $A_{\mathrm{SA/TH}}(\Delta t)$ defined through Eq. (39).

The remaining task is the reconstruction of the waveform of the MIR mode from the transformed quasiprobability distribution. As discussed in the preceding section, the sampled quadratures follow the MIR waveform if an ultrabroadband probe pulse is used. To make this argument more quantitative we consider the example of an MIR pulse with a Gaussian-mode function $f_{\tilde{\Omega}}(\Omega) = N_{\tilde{\Omega}}\sqrt{\Omega}\exp[-(\Omega-\tilde{\Omega})^2/(2\sigma_{\tilde{\Omega}})^2]$ normalized by $N_{\tilde{\Omega}}$. In this case, the coefficients

$$A_{\mathrm{SA}}(\Delta t) \approx -\mathrm{sech}(\theta)\frac{\sqrt{\Delta\tilde{\omega}}}{\theta^{(1)}_{\tilde{\omega}}}|S_c|e^{i\Phi_\perp/2}\sqrt{\frac{\pi}{n(0)}}N_{\tilde{\Omega}}\bar{\sigma}a_{(-)}(\Delta t) \tag{43}$$

and

$$\begin{aligned} A_{\mathrm{TH}}(\Delta t) \approx -\frac{\sqrt{\Delta\tilde{\omega}}}{\theta^{(1)}_{\tilde{\omega}}}|S_c|e^{i\Phi_\perp/2}\sqrt{\frac{\pi}{n(0)}}N_{\tilde{\Omega}}\bar{\sigma} \\ \times\Big[\mathrm{csch}(\theta)\ \sec(\theta_\perp)e^{-i\Phi_\perp}a_{(+)}(\Delta t) \\ -\mathrm{sech}(\theta)\tan(\theta_\perp)e^{i\Phi_\perp}a_{(-)}(\Delta t)\Big] \end{aligned} \tag{44}$$

are approximately given in terms of Gaussian profiles,

$$\begin{aligned} a_{(\mp)}(\Delta t) = \exp\left[-\frac{(\omega_p-\tilde{\omega})^2}{4\sigma_p^2}-\frac{\tilde{\Omega}^2}{4\sigma_{\tilde{\Omega}}^2}+\frac{\bar{\Omega}^2_{(\mp)}}{4\bar{\sigma}^2}\right] \\ \times\Big\{\exp[-(\Delta t-\eta_c)^2\bar{\sigma}^2-i(\Delta t-\eta_c)\bar{\Omega}_{(\mp)}] \\ -\exp[-(\Delta t+\eta_c)^2\bar{\sigma}^2-i(\Delta t+\eta_c)\bar{\Omega}_{(\mp)}]\Big\}, \end{aligned} \tag{45}$$

with the inverse-variance average $\bar{\sigma} = \sigma_p\sigma_{\tilde{\Omega}}/\sqrt{\sigma_p^2+\sigma_{\tilde{\Omega}}^2}$ and the weighted average central frequency $\bar{\Omega}_{(\mp)} = \mp(\tilde{\omega}-\omega_p)(\bar{\sigma}^2/\sigma_p^2)+\tilde{\Omega}(\bar{\sigma}^2/\sigma_{\tilde{\Omega}}^2)$. The coefficients in Eqs. (43) and (44) are obtained after approximating the phase-matching function [cf. Eq. (4)] by $S_c\mathrm{sinc}(\eta_c\Omega)$, with constant S_c given by Eq. (C4) and $\eta_c = (L/2c)[n_g(\tilde{\omega}) - n(0)]$ dependent on the group refractive index $n_g(\tilde{\omega})$. The approximation is valid as long as the refractive index of the nonlinear crystal is flat in the MIR frequency band or, in other words, dispersion is low (see Appendix C for details). The coefficients from Eqs. (43) and (44) are compared to the MIR waveform in Fig. 9 as functions of the relative time delay Δt between the NIR probe pulse and the sampled MIR mode for various probe bandwidths σ_p. Increasing the probe bandwidth improves the matching between the coefficient of the sampled mode $A_{\mathrm{SA}}(\Delta t)$ and MIR mode profile. However, as further explained below, there are six effects due to the convolution of the MIR waveform with the gating function in Eq. (40) that detrimentally affect this matching.

(1) *Desynchronization:* The most prominent effect is desynchronization between $A_{\mathrm{SA}}(\Delta t)$ and the MIR waveform by time shifts $\pm\eta_c$, also visible in the envelope of the gating function in Figs. 8(a)–8(d). The two features of the gating function are due to the oscillation of the phase-matching function in the frequency domain originating from $\sin(\eta_c\Omega) = [\exp(i\eta_c\Omega) - \exp(-i\eta_c\Omega)]/(2i)$. Convolution of the gating function with the pulsed MIR mode then leads to the $\pm\eta_c$ shifts in the time domain. If the shift is large enough (e.g., $\eta_c \gg \sigma_{\tilde{\Omega}}$), the two contributions at $-\eta_c$ and η_c do not interfere and the shift can be compensated by adjusting Δt. The shift increases with the length of the nonlinear crystal and with $\tilde{\omega}$.

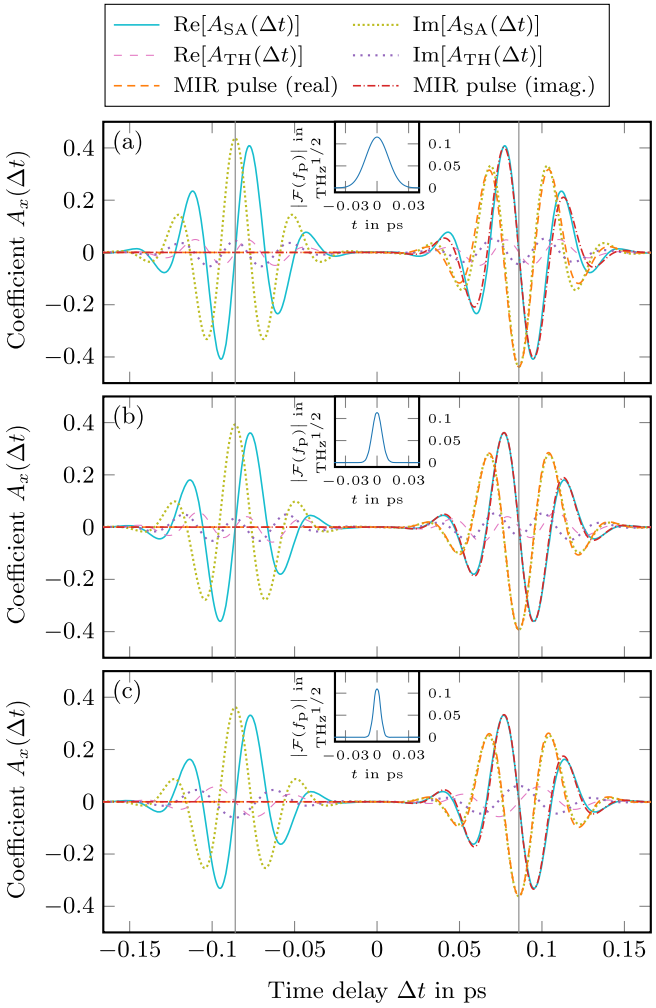

FIG. 9. Time-delay dependence of the coefficients $A_{SA}(\Delta t)$ and $A_{TH}(\Delta t)$ describing the decomposition of the MIR mode function into sampled and thermalized contributions. The filtered local oscillator is assumed to be of bandwidth $\Delta\tilde{\omega}/(2\pi) = 1$ THz and central frequency $\tilde{\omega}/(2\pi) = 300$ THz, the nonlinear crystal is of length $L = 100$ μm, and the refractive index can be taken from Eq. (C1). The sampled MIR pulse is a Gaussian of bandwidth $\sigma_{\tilde{\Omega}}/(2\pi) = 5$ THz and central frequency $\tilde{\Omega}/(2\pi) = 25$ THz and the probe of central frequency $\omega_p/(2\pi) = 350$ THz, amplitude $\alpha_p = 2 \times 10^6$, and time delay $t_p = 0$. The probe bandwidth is $\sigma_p/(2\pi) = 15$, 35, and 50 THz in (a)–(c) and the respective envelope of the probe can be seen in the inset. The dashed orange line shows the real part and the dash-dotted red line the imaginary part of the MIR pulse shape in the time domain scaled and shifted to fit $A_{SA}(\Delta t)$. The vertical line marks the point $\Delta t = \pm\eta_c$.

A proper selection of these parameters therefore allows for some degree of control over the shift. Nonetheless, for a fixed probe central frequency ω_p, the increase in $\tilde{\omega}$ makes the measurement weaker (i.e., decreases $\theta^{(1)}_{\tilde{\omega}}$) and enhances thermalization by increasing ζ_T, which can be counteracted by increasing ω_p alongside $\tilde{\omega}$. We highlight suitable values by the white dashed lines in Fig. 4.

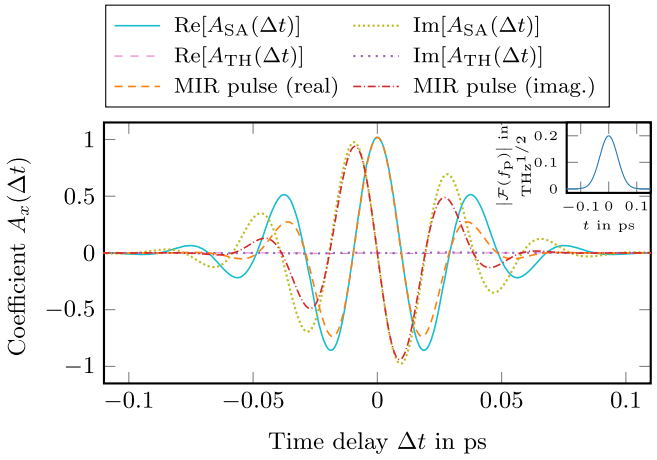

FIG. 10. Time-delay dependence of the coefficients $A_{SA}(\Delta t)$ and $A_{TH}(\Delta t)$ describing the decomposition of the mode function into sampled and thermalized contributions for different relative time delays Δt. The filtered local oscillator is of bandwidth $\Delta\tilde{\omega}/(2\pi) = 1$ THz, the central frequency is $\tilde{\omega}/(2\pi) = 300$ THz, and the refractive index given in Eq. (C1). In contrast to Fig. 9, we consider a short nonlinear crystal with $L = 6$ μm. Choosing a short crystal reduces the influence of the phase matching and allows a perfect match of the gating function $\mathcal{F}[f^*_{SA}](\Delta t)$ and the MIR waveform $\mathcal{F}[f_{\tilde{\Omega}}](\Delta t)$. The MIR sample pulse is of bandwidth $\sigma_{\tilde{\Omega}}/(2\pi) = 5$ THz, central frequency $\tilde{\Omega}/(2\pi) = 25$ THz and the probe of bandwidth $\sigma_p/(2\pi) = 5$ THz, central frequency $\omega_p/(2\pi) = 325$ THz, amplitude $\alpha_p = 2 \times 10^6$, and time delay $t_p = 0$. The envelope of the probe is shown in the inset.

(2) *Phase shifting:* The real part of $A_{SA}(\Delta t)$ corresponds to the imaginary part of the MIR waveform and vice versa, as can be seen in Fig. 9. This originates from the imaginary prefactor in the electric field and carries over to the gating function $\mathcal{F}[f^*_x](t)$. This effect is absent in Fig. 10, since the interference of the two Gaussians at $\pm\eta_c$, composing the gating function $\mathcal{F}[f^*_x](t)$, leads to an additional imaginary prefactor.

(3) *Spectral weighting:* The low-frequency end of the MIR spectrum is overestimated. This skewed spectral weighting results from the $1/\sqrt{\Omega}$ dependence of the function $f_{SA}(\Omega)$ defining the sampled mode. This effect is, however, negligible as long as the central frequency of the sampled MIR mode is large compared to its own bandwidth $\tilde{\Omega} \gg \sigma_{\tilde{\Omega}}$. This effect can be seen by comparing Figs. 9(b) and 9(c): In Fig. 9(b), $A_{SA}(\Delta t)$ seems to follow the MIR waveform better than in Fig. 9(c), even though in the latter the probe is shorter. The underestimation can be accounted for by reintroducing the factor $\sqrt{\Omega}$ in postprocessing.

(4) *Temporal averaging:* The MIR waveform is averaged over the time window defined by the gating function. For a Gaussian MIR pulsed mode with

central frequency $\tilde{\Omega}$ and variance $\sigma_{\tilde{\Omega}}$, the averaging will lead to the reconstruction of a Gaussian with an effective central frequency $\bar{\Omega}_{(-)}$ and variance $\bar{\sigma}$. When considering the limiting case of an infinitely broadband probe pulse, $\lim_{\sigma_p\to\infty}\bar{\sigma}=\sigma_{\tilde{\Omega}}$ and $\lim_{\sigma_p\to\infty}\bar{\Omega}_{(\mp)}=\tilde{\Omega}$, the reconstructed parameters tend to the actual MIR parameters, as shown in Fig. 9. This (unphysical) limit case would correspond to a probe with amplitude described by a delta distribution over time, which "averages" over a single point of the sampled mode (the instant at which they intersect). We can quantify how close the reconstructed variance and central frequency are to the corresponding MIR-pulse parameters by calculating the relative error for the variance,

$$\frac{\left|\sigma_{\tilde{\Omega}}^2-\bar{\sigma}^2\right|}{\sigma_{\tilde{\Omega}}^2}=\frac{\sigma_{\tilde{\Omega}}^2}{\sigma_{\tilde{\Omega}}^2+\sigma_p^2}, \tag{46}$$

and for the central frequency,

$$\frac{\left|\tilde{\Omega}-\bar{\Omega}_{(-)}\right|}{\tilde{\Omega}}=\left|1+\frac{\tilde{\omega}-\omega_p}{\tilde{\Omega}}\right|\frac{\sigma_{\tilde{\Omega}}^2}{\sigma_{\tilde{\Omega}}^2+\sigma_p^2}. \tag{47}$$

We see that both relative errors vanish if the bandwidth of the probe pulse considerably exceeds the MIR pulse bandwidth, $\sigma_p \gg \sigma_{\tilde{\Omega}}$. We can also see that the relative error in the central frequency is always zero when the sampled frequencies are matched to the MIR, $\omega_p-\tilde{\omega}=\tilde{\Omega}$. Using Eqs. (46) and (47) we can calculate the variance σ_p of the probe pulse required to achieve a certain relative error in the reconstructed variance and central frequency given a fixed variance and central frequency of the MIR pulse. Some exemplary values can be taken from Table I.

(5) *Thermalization:* As mentioned previously, there is an additional contribution to the signal due to the entanglement of the sampled mode with the thermalized mode $\hat{\mathrm{a}}_{\mathrm{TH}}$, which originates from the decomposition in Eq. (39) and can be observed from Fig. 9, where $A_{\mathrm{TH}}(\Delta t)$ increases with the bandwidth of the probe pulse. One could try to reduce the contribution of the thermalized mode to the MIR mode, i.e., minimize the coefficient $A_{\mathrm{TH}}(\Delta t)$ for all relative time delays Δt. A minimization of the coefficient $A_{\mathrm{TH}}(\Delta t)$ in a mathematical sense seems not feasible since the coefficient depends on the waveform of the MIR mode. However, there are two strategies to mitigate the influence of the thermalized mode. First, Eq. (44) shows that for large probe bandwidths σ_p, $a_{(+)}(\Delta t)$ and $a_{(-)}(\Delta t)$ in Eq. (45) oscillate coherently and for $\Phi_\perp=n\pi$ with $n\in\mathbb{Z}$ they interfere destructively. The latter requirement can be met by fixing the probe carrier envelope to $t_p=0$. Second, one can reduce the entanglement between the sampled and thermalized modes by decreasing the two-mode squeezing parameter ζ_T. This can be achieved by filtering below the probe central frequency, $\tilde{\omega}-\omega_p\ll 0$, as can be seen from Fig. 4. This way SFG detection is reduced, as can be seen in Fig. 3, since less of the probe bandwidth is below the filtered frequency $\tilde{\omega}$. Coincidentally, filtering below the probe central frequency will reduce the single-mode squeezing and increase the overall squeezing parameter of the nonlinear interaction $\theta_{\tilde{\omega}}^{(1)}$, as can be observed in Fig. 4. A mismatch between the central frequency of the sampled mode $\omega_p-\tilde{\omega}$ and the central frequency of the MIR mode $\tilde{\Omega}$ leads to a reduced up-conversion efficiency and in turn to a reduction of $A_{\mathrm{SA}}(\Delta t)$, but since the probe pulse is rather broadband the reduction is minor. Combining the two strategies by mismatching the sampled frequencies of the setup and the MIR central frequency to $\omega_p-\tilde{\omega}=2\tilde{\Omega}$ and fixing the carrier-envelope phase of the probe pulse, $t_p=0$, the probe can be made short enough to allow for a subcycle resolution while keeping the influence of the thermalized mode down, as can be taken from Table I. For example, under such conditions a probe pulse with bandwidth $\sigma_p/(2\pi)=35$ THz can reach a relative error in the sampled central frequency and variance of 2%, while keeping the maximum of the $A_{\mathrm{TH}}(\Delta t)$ below 13% off from the maximum of $A_{\mathrm{SA}}(\Delta t)$ [cf. Fig. 9(b)].

(6) *Deamplification:* The overlap of the gating function and the MIR waveform is imperfect. From Fig. 9, we can see that the maximum value of $A_{\mathrm{SA}}(\Delta t)$ always remains well below one. The full reconstruction of the MIR quantum state requires the coefficient $A_{\mathrm{SA}}(\Delta t)$ to be equal to one for at least one relative time delay Δt. Consider a coherent MIR sample state with amplitude α which would, if we assume no

TABLE I. Relative errors in the sampled central frequency and variance of the MIR waveform as well as the maximum of the coefficients $A_{\mathrm{SA/TH}}(\Delta t)$ in Fig. 9 for various values of the NIR probe pulse variance σ_p and a fixed MIR pulse central frequency $\tilde{\Omega}=25$ THz, variance $\sigma_{\tilde{\Omega}}/(2\pi)=5$ THz, frequency mismatch $\omega_p-\tilde{\omega}=2\tilde{\Omega}$, and a fixed carrier-envelope phase of the probe pulse $t_p=0$.

$\sigma_p/(2\pi)$	Relative error variance	Relative error central frequency	Maximum $A_{\mathrm{SA}}(\Delta t)$	Maximum $A_{\mathrm{TH}}(\Delta t)$
15 THz	10%	10%	0.44	0.02
35 THz	2%	2%	0.39	0.05
50 THz	1%	1%	0.36	0.06

thermalization, appear to our measurement setup as a coherent state with amplitude $A_{\mathrm{SA}}(\Delta t)\alpha$. Thus, to reconstruct α, $A_{\mathrm{SA}}(\Delta t)$ needs to be one for some Δt. In other words, the sampled mode function, defined by $f_{\mathrm{SA}}(\Omega)$, has to coincide with that of the MIR pulsed mode, defined by $f_{\tilde{\Omega}}(\Omega)$. In this case, in the absence of any relative time delay, $\Delta t = 0$, the coefficient becomes one, $A_{\mathrm{SA}}(\Delta t = 0) = \mathcal{F}[f_{\tilde{\Omega}} f_{\mathrm{SA}}^*](\Delta t = 0) = \int_0^\infty |f_{\tilde{\omega}}(\Omega)|^2 \mathrm{d}\Omega = 1$. This can be achieved approximately by choosing $\sigma_{\mathrm{p}} = \sigma_{\tilde{\Omega}}$ and $\omega_{\mathrm{p}} - \tilde{\omega} = \tilde{\Omega}$. Furthermore, the nonlinear crystal has to be sufficiently small to suppress the influence of the phase matching, as can be seen from the approximation (and $\eta_{\mathrm{c}} \propto L$)

$$|A_{\mathrm{SA}}(\Delta t = 0)| \approx \exp(-\eta_{\mathrm{c}}^2 \sigma_{\tilde{\Omega}}^2/2)\mathrm{sinc}(\eta_{\mathrm{c}}\tilde{\Omega}), \tag{48}$$

which is valid as long as the probe pulse and MIR sample pulse spectrum overlap and dispersion is low in the MIR range. For $\sigma_{\tilde{\Omega}}/(2\pi) = 5$ THz, $(\omega_{\mathrm{p}} - \tilde{\omega})/(2\pi) = \tilde{\Omega}/(2\pi) = 25$ THz, and $\tilde{\omega}/(2\pi) = 300$ THz, the nonlinear crystal has to be $L = 6$ μm for $|A_{\mathrm{SA}}(\Delta t)|$ to reach a maximum of 0.8 if the approximated expression in Eq. (48) is used [precise numerical evaluation of Eq. (43) results in a maximum of 0.99]. Numerical data on the coefficient $A_{\mathrm{SA}}(\Delta t)$ for the previously mentioned values is shown in Fig. 10.

V. CONCLUSIONS

In this work we propose an electro-optic-based tomography scheme able to reconstruct a time-dependent quantum state in the midinfrared range, allowing for a dynamical sampling of spatiotemporally localized optical modes not only in phase space but also in the time domain with subcycle resolution. Utilizing two recently developed theoretical tools [54,66], we derive the photon-count probability distribution $p(\{\Delta n_i\})$ for multichannel subcycle quantum electro-optic sampling and show how this quantity is related to a specific time-dependent phase-space distribution of the sampled state. We scrutinize the physical sources of noise in the quantum electro-optic signal variance and show that sampling nonmonochromatic optical modes with subcycle resolution leads to two intriguing effects that detrimentally enhance the noise: a state-independent contribution scaling with the interaction strength between the sampled MIR and the detected NIR modes and thermalization noise due to entanglement breaking between the sampled and unsampled modes. The latter effect is unparalleled by continuous-wave-driven multichannel electro-optic sampling, which is mostly limited by noise due to the simultaneous measurement of noncommuting observables. We then propose a scheme to minimize the thermalization noise by a mismatch between the central frequencies of the probe pulse used to drive the nonlinear interaction and of the detected NIR modes. Finally, we demonstrate the reconstruction of the waveform using the example of a Gaussian midinfrared pulsed mode. Our proposed optical tomography scheme is able to dynamically sample a broadband quantum state using an ultrabroadband probe pulse, opening a new paradigm for time-domain quantum tomography with subcycle resolution.

Note added. Recently, we became aware of several related works [79–81].

ACKNOWLEDGMENTS

We acknowledge funding by the Deutsche Forschungsgemeinschaft (DFG)—Project No. 425217212—SFB 1432. T. L. M. G. gratefully acknowledges the funding by the Baden-Württemberg Stiftung via the Elite Programme for Postdocs. T. L. M. G. also acknowledges support by the ERC Starting Grant QNets through Grant No. 804247.

APPENDIX A: TWO-MODE CHARACTERISTIC FUNCTION

In this appendix we derive the relation used in Eq. (38) between the two-mode and single-mode characteristic function. The eigenstates of the operators $\{\hat{\mathbf{u}}_{\tilde{\omega}_i} | i = X, Y\} \cup \{\hat{\mathbf{a}}_{\mathrm{SA}}, \hat{\mathbf{a}}_{\mathrm{TH}}\}$ span the Hilbert space of electro-optic sampling (EOS) $\mathcal{H}_{\mathrm{EOS}} = (\bigotimes_{i=X,Y} \mathcal{H}_{\tilde{\omega}_i}) \otimes \mathcal{H}_{\mathrm{SA}} \otimes \mathcal{H}_{\mathrm{TH}}$ which is a factor of the uncountably infinite dimensional Hilbert space $\mathcal{H} = \mathcal{H}_{\mathrm{EOS}} \otimes \mathcal{H}_{\mathrm{r}}$. By defining the reduced density operator $\hat{\rho}_{\mathrm{TM}} = \mathrm{tr}_{\mathrm{r}}(\hat{\rho}_{\tilde{\Omega}})$ of the two broadband modes, we can see that the electro-optic signal inherits contributions from (unsampled) modes correlated to the sampled modes. The density operator $\hat{\rho}_{\mathrm{TM}}$ acts on the effective bipartite Hilbert space $\mathcal{H}_{\mathrm{SA}} \otimes \mathcal{H}_{\mathrm{TH}}$ and can hence be written in terms of the displacement operators $\hat{D}_{\mathrm{SA}}(\beta_{\mathrm{SA}})$ and $\hat{D}_{\mathrm{TH}}(\beta_{\mathrm{TH}})$ generated by $\hat{\mathbf{a}}_{\mathrm{SA}}$ and $\hat{\mathbf{a}}_{\mathrm{TH}}$ (see Ref. [82], p. 265):

$$\hat{\rho}_{\mathrm{TM}} = \frac{1}{\pi^2} \int \chi_{\mathrm{TM}}(\beta_{\mathrm{SA}}, \beta_{\mathrm{TH}}) \hat{D}_{\mathrm{SA}}^\dagger(\beta_{\mathrm{SA}}) \times \hat{D}_{\mathrm{TH}}^\dagger(\beta_{\mathrm{TH}}) \mathrm{d}^2\beta_{\mathrm{SA}} \mathrm{d}^2\beta_{\mathrm{TH}}, \tag{A1}$$

with the symmetrically ordered, two-mode characteristic function,

$$\chi_{\mathrm{TM}}(\beta_{\mathrm{SA}}, \beta_{\mathrm{TH}}) = \left\langle \hat{D}_{\mathrm{SA}}(\beta_{\mathrm{SA}}) \hat{D}_{\mathrm{TH}}(\beta_{\mathrm{TH}}) \right\rangle_{\hat{\rho}_{\mathrm{TM}}}. \tag{A2}$$

However, as we have already seen, the effective nonlinear unitary operator Eq. (29) acts only on the subspace $(\bigotimes_{i \in I} \mathcal{H}_{\tilde{\omega}_i}) \otimes \mathcal{H}_{\mathrm{SA}}$. Thus, we have to calculate the transformed and reduced density operator on the Hilbert space $\mathcal{H}_{\mathrm{SA}}$,

$$\hat{\tilde{\rho}}_{\mathrm{SA}} = \mathrm{tr}_{\mathrm{TH}}\left[\hat{T}^\dagger \hat{S}^\dagger \hat{\rho}_{\mathrm{TM}} \hat{S}\, \hat{T}\right] = \frac{1}{\pi}\int \chi_{\mathrm{SA}}(\beta)\hat{D}^\dagger_{\mathrm{SA}}(\beta)\mathrm{d}^2\beta, \tag{A3}$$

with the symmetrically ordered characteristic function $\chi_{\mathrm{SA}}(\beta) = \left\langle \hat{D}_{\mathrm{SA}}(\beta)\right\rangle_{\hat{\tilde{\rho}}_{\mathrm{SA}}}$. Inserting Eq. (A1) into Eq. (A3) leads to

$$\hat{\tilde{\rho}}_{\mathrm{SA}} = \frac{1}{\pi^2}\int \chi_{\mathrm{TM}}(\beta_{\mathrm{SA}},\beta_{\mathrm{TH}})\mathrm{tr}_{\mathrm{TH}}\left[\hat{T}^\dagger \hat{S}^\dagger \hat{D}^\dagger_{\mathrm{SA}}(\beta_{\mathrm{SA}})\hat{D}^\dagger_{\mathrm{TH}}(\beta_{\mathrm{TH}})\hat{S}\, \hat{T}\right]\mathrm{d}^2\beta_{\mathrm{SA}}\mathrm{d}^2\beta_{\mathrm{TH}}. \tag{A4}$$

Apply the single-mode squeezing operator leads to

$$\hat{S}^\dagger \hat{D}_{\mathrm{SA}}(\beta_{\mathrm{SA}})\hat{S} = \hat{D}_{\mathrm{SA}}(\tilde{\beta}_{\mathrm{SA}}), \tag{A5}$$

with $\tilde{\beta}_{\mathrm{SA}} = \mu_{\mathrm{S}}\beta_{\mathrm{SA}} - \nu_{\mathrm{S}}\beta^*_{\mathrm{SA}}$. Thus, with the Jacobian determinant $\det\left[D\tilde{\beta}_{\mathrm{SA}}\right] = \mu_{\mathrm{S}}^2 - |\nu_{\mathrm{S}}|^2 = 1$, we can write the reduced density operator as follows:

$$\hat{\tilde{\rho}}_{\mathrm{SA}} = \frac{1}{\pi^2}\int \chi_{\mathrm{TM}}(\mu_{\mathrm{S}}\tilde{\beta}_{\mathrm{SA}} - \nu_{\mathrm{S}}\tilde{\beta}^*_{\mathrm{SA}},\beta_{\mathrm{TH}})\mathrm{tr}_{\mathrm{TH}}\left[\hat{T}^\dagger \hat{D}^\dagger_{\mathrm{SA}}(\tilde{\beta}_{\mathrm{SA}})\hat{T}\hat{T}^\dagger \hat{D}^\dagger_{\mathrm{TH}}(\beta_{\mathrm{TH}})\hat{T}\right]\mathrm{d}^2\tilde{\beta}_{\mathrm{SA}}\mathrm{d}^2\beta_{\mathrm{TH}}. \tag{A6}$$

If we now apply the two-mode squeezing operators on the displacement operators,

$$\begin{aligned}\hat{T}^\dagger \hat{D}_{\mathrm{TH}}(\tilde{\beta}_{\mathrm{TH}})\hat{T} &= \exp\left\{\beta_{\mathrm{TH}}\left[\mu_{\mathrm{T}}\hat{\mathfrak{a}}^\dagger_{\mathrm{TH}} - \nu_{\mathrm{T}}\hat{\mathfrak{a}}_{\mathrm{SA}}\right] - \mathrm{H.c.}\right\} \\ &= \hat{D}_{\mathrm{TH}}(\mu_{\mathrm{T}}\beta_{\mathrm{TH}}) \otimes \hat{D}_{\mathrm{SA}}(\nu_{\mathrm{T}}\beta^*_{\mathrm{TH}}),\end{aligned} \tag{A7}$$

$$\begin{aligned}\hat{T}^\dagger \hat{D}_{\mathrm{SA}}(\tilde{\beta}_{\mathrm{SA}})\hat{T} &= \exp\left\{\tilde{\beta}_{\mathrm{SA}}\left[\mu_{\mathrm{T}}\hat{\mathfrak{a}}^\dagger_{\mathrm{SA}} - \nu_{\mathrm{T}}\hat{\mathfrak{a}}_{\mathrm{TH}}\right] - \mathrm{H.c.}\right\} \\ &= \hat{D}_{\mathrm{TH}}(\nu_{\mathrm{T}}\tilde{\beta}^*_{\mathrm{SA}}) \otimes \hat{D}_{\mathrm{SA}}(\mu_{\mathrm{T}}\tilde{\beta}_{\mathrm{SA}}).\end{aligned} \tag{A8}$$

Using the fact that the trace over the displacement operator gives a delta distribution (Ref. [82], p. 339),

$$\mathrm{tr}_{\mathrm{TH}}\left\{\hat{D}_{\mathrm{TH}}[\mu_{\mathrm{T}}\beta_{\mathrm{TH}}]\hat{D}_{\mathrm{TH}}\left[\nu_{\mathrm{T}}(\tilde{\beta}_{\mathrm{SA}})^*\right]\right\} = \frac{\pi}{(\mu_{\mathrm{T}})^2}\delta\left[\mathrm{Re}(\beta_{\mathrm{TH}}) + \frac{\nu_{\mathrm{T}}}{\mu_{\mathrm{T}}}\mathrm{Re}(\tilde{\beta}_{\mathrm{SA}})\right]\delta\left[\mathrm{Im}(\beta_{\mathrm{TH}}) - \frac{\nu_{\mathrm{T}}}{\mu_{\mathrm{T}}}\mathrm{Im}(\tilde{\beta}_{\mathrm{SA}})\right], \tag{A9}$$

the reduced and transformed density operator can thus be written as follows:

$$\begin{aligned}\hat{\tilde{\rho}}_{\mathrm{SA}} &= \frac{1}{\pi^2}\iint \chi_{\mathrm{TM}}\left(\mu_{\mathrm{S}}\tilde{\beta}_{\mathrm{SA}} - \nu_{\mathrm{S}}\tilde{\beta}^*_{\mathrm{SA}},\beta_{\mathrm{TH}}\right)\mathrm{tr}_{\mathrm{TH}}\left[\hat{D}_{\mathrm{TH}}(-\mu_{\mathrm{T}}\beta_{\mathrm{TH}})\hat{D}_{\mathrm{TH}}\left(-\nu_{\mathrm{T}}\tilde{\beta}^*_{\mathrm{SA}}\right)\right]\hat{D}_{\mathrm{SA}}(-\nu_{\mathrm{T}}\beta^*_{\mathrm{TH}})\hat{D}_{\mathrm{SA}}\left(-\mu_{\mathrm{T}}\tilde{\beta}_{\mathrm{SA}}\right)\mathrm{d}^2\beta_{\mathrm{TH}}\mathrm{d}^2\tilde{\beta}_{\mathrm{SA}} \\ &= \frac{1}{\pi\mu_{\mathrm{T}}^2}\int \chi_{\mathrm{TM}}\left(\mu_{\mathrm{S}}\tilde{\beta}_{\mathrm{SA}} - \nu_{\mathrm{S}}\tilde{\beta}^*_{\mathrm{SA}}, -\frac{\nu_{\mathrm{T}}}{\mu_{\mathrm{T}}}\tilde{\beta}^*_{\mathrm{SA}}\right)\hat{D}_{\mathrm{SA}}(-\nu_{\mathrm{T}}\beta^*_{\mathrm{TH}})\hat{D}_{\mathrm{SA}}\left(-\mu_{\mathrm{T}}\tilde{\beta}_{\mathrm{SA}}\right)\mathrm{d}^2\tilde{\beta}_{\mathrm{SA}} \\ &= \frac{1}{\pi}\int \chi_{\mathrm{TM}}\left[\mu_{\mathrm{T}}\left(\mu_{\mathrm{S}}\tilde{\beta}_{\mathrm{SA}} - \nu_{\mathrm{S}}\tilde{\beta}^*_{\mathrm{SA}}\right), -\nu_{\mathrm{T}}\tilde{\beta}^*_{\mathrm{SA}}\right]\hat{D}_{\mathrm{SA}}\left(-\tilde{\beta}_{\mathrm{SA}}\right)\mathrm{d}^2\tilde{\beta}_{\mathrm{SA}} \\ &= \frac{1}{\pi}\int \chi_{\mathrm{SA}}(\beta)\hat{D}_{\mathrm{SA}}(-\beta)\mathrm{d}^2\beta.\end{aligned} \tag{A10}$$

Comparing the last two lines, we can conclude that

$$\chi_{\mathrm{SA}}(\beta) = \chi_{\mathrm{TM}}[\mu_{\mathrm{T}}(\mu_{\mathrm{S}}\beta - \nu_{\mathrm{S}}\beta^*), -\nu_{\mathrm{T}}\beta^*]. \tag{A11}$$

As an alternative approach to the spectral splitting using a prism, applying a beam splitter after the spectral filtering can also implement the simultaneous measurement. The time evolution in Eq. (11) has to be modified to

$$\hat{U} = \hat{U}_{\mathrm{WP}}\hat{D}_{\vec{\omega}}(\vec{\beta})\hat{U}_{\mathrm{B}}\hat{U}_{\mathrm{NL}}, \tag{A12}$$

with the operator $\hat{U}_{\mathrm{B}} = \exp[\mathrm{i}(\pi/4)(\hat{u}^\dagger_{\tilde{\omega}_X}\hat{u}_{\tilde{\omega}_Y} + \mathrm{H.c.})]$. Since the beam splitter has no effect on the vacuum, it can be inserted into Eq. (32) resulting in

$$p(\{\Delta n_i\}) = \mathrm{tr}\left(\hat{P}_{\{\Delta n_i\}}\hat{U}\hat{U}_{\mathrm{B}^\dagger}\hat{\rho}_{\vec{\Omega}} \otimes |0\rangle_{\mathrm{NIR\ NIR}}\langle 0|\hat{U}_{\mathrm{B}}\hat{U}^\dagger\right). \tag{A13}$$

Applying the beam splitter to the nonlinear operator, $\hat{U}_{\mathrm{B}}\hat{U}_{\mathrm{NL}}\hat{U}_{\mathrm{B}}^{\dagger}$, will result in a similar decomposition as Eq. (10) with $\tilde{\alpha}_X = 1/\sqrt{2}$ and $\tilde{\alpha}_Y = \mathrm{i}/\sqrt{2}$. The additional imaginary unit can be accounted for by tuning the wave plates according to the result from Ref. [66]. This alternative approach promotes the electro-optic-sampling setup proposed in Ref. [45] to a quantum tomography protocol.

APPENDIX B: QUASIPROBABILITY DISTRIBUTION FOR VARIOUS STATES

In this appendix we present the transformed (s_X, s_Y)-quasiprobability distributions for different states. The (s_X, s_Y)-quasiprobability distributions are a generalization of the s-quasiprobability distributions (see Ref. [66] for details), which can be recovered through $s = s_X = s_Y$.

1. Coherent states

Starting with a coherent MIR input state, $\hat{\rho}_{\tilde{\Omega}} = \hat{D}_{\tilde{\Omega}}(\alpha_{\tilde{\Omega}})|0\rangle\langle 0|\hat{D}_{\tilde{\Omega}}^{\dagger}(\alpha_{\tilde{\Omega}})$, generated by $\hat{D}_{\tilde{\Omega}}(\alpha_{\tilde{\Omega}}) = \exp\left(\alpha_{\tilde{\Omega}}\int_0^{\infty} f_{\tilde{\Omega}}^{*}(\Omega)\hat{a}_{\Omega}^{\dagger}\mathrm{d}\Omega - \mathrm{H.c.}\right)$, and using $A_1(\Delta t) = \mu_{\mathrm{T}}\mu_{\mathrm{S}}A_{\mathrm{SA}}(\Delta t)$, $A_2 = \mu_{\mathrm{T}}\nu_{\mathrm{S}}^{*}A_{\mathrm{SA}}(\Delta t) + \nu_{\mathrm{T}}A_{\mathrm{TH}}(\Delta t)$, as well as

$$\sigma_X^2 = \frac{1}{2}(\mu_{\mathrm{TH}}^2|\mu_{\mathrm{S}} - \nu_{\mathrm{S}}|^2 + \nu_{\mathrm{T}}^2 - s_X), \tag{B1}$$

$$\sigma_Y^2 = \frac{1}{2}(\mu_{\mathrm{T}}^2|\mu_{\mathrm{S}} + \nu_{\mathrm{S}}|^2 + \nu_{\mathrm{T}}^2 - s_Y), \tag{B2}$$

$$\sigma_{XY}^2 = \mu_{\mathrm{T}}^2\mu_{\mathrm{S}}|\nu_{\mathrm{S}}|\sin(\Phi_{\perp}), \tag{B3}$$

the quasiprobability distribution of a coherent state can be expressed as

$$\begin{aligned}\tilde{\rho}_{\mathrm{SA}}(z; s_X, s_Y|\alpha_{\tilde{\Omega}}) = [\sigma_X^2\sigma_Y^2 - \sigma_{XY}^4]^{-1/2}\exp\Big[\{-\mathrm{Re}^2([A_1(\Delta t) + A_2(\Delta t)]\alpha_{\tilde{\Omega}} - z)\sigma_X^2 - \mathrm{Im}^2([A_1(\Delta t) - A_2(\Delta t)]\alpha_{\tilde{\Omega}} - z)\sigma_Y^2 \\ - 2\mathrm{Re}([A_1(\Delta t) + A_2(\Delta t)]\alpha_{\tilde{\Omega}} - z)\mathrm{Im}([A_1(\Delta t) - A_2(\Delta t)]\alpha_{\tilde{\Omega}} - z)\sigma_{XY}^2\}/\{\sigma_X^2\sigma_Y^2 - \sigma_{XY}^4\}\Big].\end{aligned} \tag{B4}$$

2. Cat states

Next, let us assume the MIR modes are in a cat state $\hat{\rho}_{\tilde{\Omega}} = |\mathrm{cat}\rangle\langle\mathrm{cat}|$ with $|\mathrm{cat}\rangle = N_{\mathrm{cat}}[\hat{D}_{\tilde{\Omega}}(\alpha_{\tilde{\Omega}}) + \hat{D}_{\tilde{\Omega}}(-\alpha_{\tilde{\Omega}})]|0\rangle$ and $N_{\mathrm{cat}} = (2 + 2e^{-2|\alpha_{\tilde{\Omega}}|^2})^{-1/2}$, the transformed quasiprobability distribution is

$$\tilde{\rho}_{\mathrm{SA}}(z; s_X, s_Y|\mathrm{cat}) = N_{\mathrm{cat}}^2\Big[\tilde{\rho}_{\mathrm{SA}}(z; s_X, s_Y|\alpha_{\tilde{\Omega}}) + \tilde{\rho}_{\mathrm{SA}}(z; s_X, s_Y| - \alpha_{\tilde{\Omega}}) + \exp\Big(-2|A_{\mathrm{UN}}(\Delta t)\alpha_{\tilde{\Omega}}|^2\Big)\rho_{\mathrm{osc}}(z; s_X, s_Y)\Big], \tag{B5}$$

with

$$\begin{aligned}\rho_{\mathrm{osc}}(z; s_X, s_Y) = 2\tilde{\rho}_{\mathrm{SA}}(z; s_X, s_Y|\mathrm{vac})\exp\Big[(|A_{\mathrm{UN}}(\Delta t)|^2 - 1)2|\alpha_{\tilde{\Omega}}|^2 \\ + \Big(\mathrm{Re}^2\{[A_1(\Delta t) - A_2(\Delta t)]\alpha_{\tilde{\Omega}}\}\sigma_Y^2 + \mathrm{Im}^2\{[A_1(\Delta t) + A_2(\Delta t)]\alpha_{\tilde{\Omega}}\}\sigma_X^2 \\ - 2\mathrm{Re}\{[A_1(\Delta t) - A_2(\Delta t)]\alpha_{\tilde{\Omega}}\}\mathrm{Im}\{[A_1(\Delta t) + A_2(\Delta t)]\alpha_{\tilde{\Omega}}\}\sigma_{XY}^2\Big)/(\sigma_X^2\sigma_Y^2 - \sigma_{XY}^4)\Big] \\ \times\cos\Big\{2\Big[\Big(\mathrm{Im}\{[A_1(\Delta t) + A_2(\Delta t)]\alpha_{\tilde{\Omega}}\}\sigma_X^2 - \mathrm{Re}([A_1(\Delta t) - A_2(\Delta t)]\alpha_{\tilde{\Omega}})\sigma_{XY}^2\Big)\mathrm{Re}(z) \\ + (\mathrm{Re}([A_1(\Delta t) - A_2(\Delta t)]\alpha_{\tilde{\Omega}})\sigma_Y^2 - \mathrm{Im}([A_1(\Delta t) + A_2(\Delta t)]\alpha_{\tilde{\Omega}})\sigma_{XY}^2)\mathrm{Im}(z)\Big]/[\sigma_X^2\sigma_Y^2 - \sigma_{XY}^4]\Big\}\Big).\end{aligned} \tag{B6}$$

3. Squeezed states

If the MIR-input state is in the squeezed vacuum $\hat{\rho}_{\tilde{\Omega}} = \hat{S}_{\tilde{\Omega}}(\zeta_{\tilde{\Omega}})|0\rangle\langle 0|\hat{S}_{\tilde{\Omega}}^{\dagger}(\zeta_{\tilde{\Omega}})$, generated by

$$\hat{S}_{\tilde{\Omega}}(\alpha_{\tilde{\Omega}}) = \exp\Big[\frac{1}{2}\zeta_{\tilde{\Omega}}^{*}\Big(\int_0^{\infty} f_{\tilde{\Omega}}(\Omega)\hat{a}_{\Omega}\mathrm{d}\Omega\Big)^2 - \mathrm{H.c.}\Big], \tag{B7}$$

and using $A_1 = \mu_{\mathrm{T}}\mu_{\mathrm{S}}A_{\mathrm{SA}}$, $A_2 = \mu_{\mathrm{T}}\nu_{\mathrm{S}}A_{\mathrm{SA}} + \nu_{\mathrm{T}}A_{\mathrm{TH}}$, as well as

$$\sigma_X^2 = \frac{1}{2}(\mu_{\mathrm{T}}^2|\mu_{\mathrm{S}} + \nu_{\mathrm{S}}|^2 + \nu_{\mathrm{T}}^2 - s_X) + \mathrm{Re}(\mu_{\tilde{\Omega}}\nu_{\tilde{\Omega}}^{*}(A_1 - A_2)^2) + |\nu_{\tilde{\Omega}}|^2|A_1 - A_2|^2, \tag{B8}$$

$$\sigma_Y^2 = \frac{1}{2}(\mu_T^2|\mu_S - \nu_S|^2 + \nu_T^2 - s_Y) - \mathrm{Re}(\mu_{\tilde{\Omega}}\nu_{\tilde{\Omega}}^*(A_1 + A_2)^2) + |\nu_{\tilde{\Omega}}|^2|A_1 + A_2|^2, \tag{B9}$$

$$\sigma_{XY}^2 = \mu_T^2\mu_S|\nu_S|\sin(\Phi_\perp) + \mu_{\tilde{\Omega}}[\mathrm{Im}(\nu_{\tilde{\Omega}}^* A_1^2) - \mathrm{Im}(\nu_{\tilde{\Omega}}^* A_2^2)] + 2|\nu_{\tilde{\Omega}}|^2\mathrm{Im}(A_1 A_2^*), \tag{B10}$$

the quasiprobability distribution takes a similar form to the coherent state, as the coherent states are squeezed by the interaction in the nonlinear crystal:

$$\tilde{\rho}_{SA}(z; s_X, s_Y|\zeta_{\tilde{\Omega}}) = [\sigma_X^2\sigma_Y^2 - \sigma_{XY}^4]^{-1/2}\exp\Big[\{-\mathrm{Re}^2(z)\sigma_X^2 - \mathrm{Im}^2(z)\sigma_Y^2 - 2\mathrm{Re}(z)\mathrm{Im}(z)\sigma_{XY}^2\}/\{\sigma_X^2\sigma_Y^2 - \sigma_{XY}^4\}\Big]. \tag{B11}$$

APPENDIX C: APPROXIMATE SOLUTION TO THE COEFFICIENTS

In this appendix we derive an approximate solution for the coefficients $A_{SA}(\Delta t)$ and $A_{TH}(\Delta t)$. The approximation is based on the assumption that, for the sampled MIR-frequency range, the refractive index of the nonlinear crystal is sufficiently flat. We use a simplified model for the refractive index of zinc telluride given by

$$\begin{aligned} n_\omega = {} & \Theta[b - |\omega|/(2\pi)](a_1|\omega| + c_1) \\ & + \Theta[|\omega|/(2\pi) - b](a_2[|\omega| - b]^2 + c_2), \end{aligned} \tag{C1}$$

with $b = 140\,\mathrm{THz}$, $a_1 = 3.5\times10^{-4}\,\mathrm{ps}$, $a_2 = 2.6\times10^{-6}\,\mathrm{ps}^2$, $c_1 = 2.55$, $c_2 = 2.75$, and Θ being the Heaviside step function. The model is based on data from Ref. [44] for the MIR range and on Ref. [83] for the NIR. In the MIR range the refractive index is flat, as can be seen in Fig. 11. Using $\Omega n_\Omega = ck_\Omega$ we can expand $k_{\tilde{\omega}-\Omega} \approx k_{\tilde{\omega}} - (\mathrm{d}k_\omega/\mathrm{d}\omega)|_{\omega=\tilde{\omega}}\Omega = k_{\tilde{\omega}} - [n_g(\tilde{\omega})/c]\Omega$ to first order, where

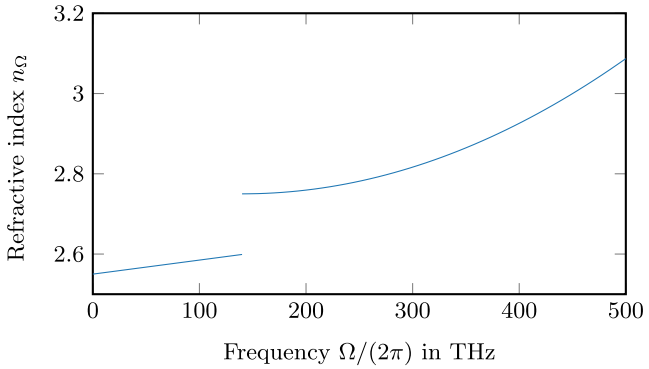

FIG. 11. A simple model for the refractive index of zinc telluride. This was obtained by combining the data from Ref. [44] for the MIR range and data from Ref. [83] for the NIR. In the MIR range a linear relation is assumed, while in the NIR it is assumed to be quadratic.

$n_g(\tilde{\omega})$ is the group refractive index at $\tilde{\omega}$, if $|\mathrm{d}k_\Omega/\mathrm{d}\Omega||_{\omega=\tilde{\omega}} \gg \frac{1}{2}|\mathrm{d}^2k_\Omega/\mathrm{d}\Omega^2|_{\omega=\tilde{\omega}}\Omega|$ for small Ω we can expand $(\tilde{\omega} - \Omega)n_{\tilde{\omega}-\Omega} = k_{\tilde{\omega}-\Omega}c$ to first order. Now we can approximate the frequency of the phase-matching function,

$$\eta_{\tilde{\omega},\Omega} \approx \frac{L\Omega}{2c}[n_g - n(\Omega)] \approx \frac{L\Omega}{2c}[n_g(\tilde{\omega}) - n(0)] = \eta_c\Omega, \tag{C2}$$

with the period of the phase-matching function $\eta_c = (L/2c)[n_g(\tilde{\omega}) - n(0)]$. Furthermore, using

$$E_p(\omega) \approx \mathrm{i}\left(\frac{\hbar}{4\pi c\varepsilon_0 A}\right)^{1/2}\sqrt{\frac{|\omega_p|}{n_{\omega_p}}}f_p(\omega), \tag{C3}$$

and defining

$$S_c = -\frac{\mathrm{i}}{\hbar}\left(\mathrm{i}\sqrt{\frac{\hbar}{4\pi c\varepsilon_0 A}}\right)^3\left(-4\pi L\frac{A\varepsilon_0 d}{2}\right)\sqrt{\frac{\tilde{\omega}}{n_{\tilde{\omega}}}}\alpha_p{}^*\sqrt{\frac{\omega_p}{n_{\omega_p}}}\frac{1}{\eta_c}, \tag{C4}$$

the joint spectral amplitude can be written as

$$S(\Omega, \tilde{\omega}) \approx S_c f_p(\tilde{\omega} - \Omega)\mathrm{sgn}(\Omega)\sqrt{\frac{|\Omega|}{n(0)}}\frac{1}{\Omega}\sin(\eta_c\Omega). \tag{C5}$$

The above approximation of Eq. (C5) allows us to analytically solve the integrals for the coefficients $A_{SA}(\Delta t)$ and $A_{TH}(\Delta t)$ defined through Eq. (39) using $\mathrm{erfcx}(z) = \exp(z^2)[1 - \mathrm{erf}(z)]$ resulting in

$$\begin{aligned} A_{SA} \approx {} & \mathrm{sech}(\theta)\frac{\sqrt{\Delta\tilde{\omega}}}{\theta_{\tilde{\omega}}^{(1)}}S_c e^{-\mathrm{i}\tilde{\omega}t_p}\sqrt{\frac{1}{n(0)}}N_{\tilde{\Omega}}\frac{1}{2\mathrm{i}}\sqrt{\pi}\bar{\sigma} \\ & \times \exp\Big[-(\omega_p - \tilde{\omega})^2/(4\sigma_p^2) - \tilde{\Omega}^2/(4\sigma_{\tilde{\Omega}}^2)\Big] \\ & \times \Big\{\mathrm{erfcx}[\mathrm{i}(\Delta t - \eta_c)\bar{\sigma} - \bar{\Omega}_{SA}\bar{\sigma}] \\ & - \mathrm{erfcx}[\mathrm{i}(\Delta t + \eta_c)\bar{\sigma} - \bar{\Omega}_{SA}\bar{\sigma}]\Big\}, \end{aligned} \tag{C6}$$

$$A_{\mathrm{TH}} \approx \sec(\theta_\perp)\mathrm{csch}(\theta)\frac{\sqrt{\Delta\tilde{\omega}}}{\theta^{(1)}_{\tilde{\omega}}} S^*_{\mathrm{c}} e^{i\tilde{\omega}t_{\mathrm{p}}}\sqrt{\frac{1}{n(0)}} N_{\tilde{\Omega}}\frac{1}{2\mathrm{i}}\sqrt{\pi}\bar{\sigma} \times \exp\left[-(\omega_{\mathrm{p}}-\tilde{\omega})^2/(4\sigma_{\mathrm{p}}^2) - \tilde{\Omega}^2/(4\sigma_{\tilde{\Omega}}^2)\right] \times \Big\{\mathrm{erfcx}[\mathrm{i}(\Delta t-\eta_{\mathrm{c}})\bar{\sigma} - \bar{\Omega}_{\mathrm{TH}}\bar{\sigma}] - \mathrm{erfcx}[\mathrm{i}(\Delta t+\eta_{\mathrm{c}})\bar{\sigma} - \bar{\Omega}_{\mathrm{TH}}\bar{\sigma}]\Big\} - \tan(\theta_\perp)e^{i\Phi_\perp}A_{\mathrm{SA}}. \tag{C7}$$

Since $f_{\tilde{\Omega}}(\Omega)\approx 0$ for $\Omega \le 0$, we can expand the integral over the frequencies over the whole real numbers, resulting in the Fourier transform in Eq. (40) and thus in Eqs. (43) and (44). Furthermore, we assume $\alpha_{\mathrm{p}} \in \mathbb{R}$ and obtain $\Phi_\perp = \pi - 2\tilde{\omega}t_{\mathrm{p}}$.

APPENDIX D: DETAILS TO THE THERMALIZATION NOISE

Using the framework developed in Ref. [66], we can relate the (ensemble) expectation values of the photon-count differences Δn_i (for $i = X, Y$) to the nonmonochromatic MIR quadratures $\hat{\mathfrak{X}}_{\mathrm{SA}}(\varphi) = \frac{1}{2}(\hat{\mathfrak{a}}_{\mathrm{SA}}e^{i\varphi} + \hat{\mathfrak{a}}^\dagger_{\mathrm{SA}}e^{-i\varphi})$ with $\varphi_X = 0$ and $\varphi_Y = -\pi/2$ by

$$\langle \Delta n_i\rangle_{\hat{\tilde{\rho}}_{\mathrm{SA}}} \approx \sqrt{2}\sinh\left(|\theta^{(1)}_{\tilde{\omega}}|\right)|\beta_Q|\left\langle \hat{\mathfrak{X}}_{\mathrm{SA}}(\varphi_i)\right\rangle_{\hat{\tilde{\rho}}_{\mathrm{SA}}}. \tag{D1}$$

Similarly, the (root mean square) variances of the photon-number differences can be related to the variances of the quadratures, $\sigma^2_{\hat{\mathfrak{X}}_{\mathrm{SA}}(\varphi_i)} = \langle \hat{\mathfrak{X}}^2_{\mathrm{SA}}(\varphi_i)\rangle - \langle \hat{\mathfrak{X}}_{\mathrm{SA}}(\varphi_i)\rangle^2$, according to [66]

$$\sigma^2_{\Delta n_i} \approx 2\sinh^2(|\theta^{(1)}_{\tilde{\omega}}|)|\beta_i|^2\left(\sigma^2_{\hat{\mathfrak{X}}_{\mathrm{SA}}(\varphi_i)}|_{\hat{\tilde{\rho}}_{\mathrm{SA}}} - \frac{\tilde{s}}{4}\right). \tag{D2}$$

The variance has two contributions, one dependent on the MIR state and one dependent only on the parameter of the nonlinear interaction $\tilde{s} = 1 - 2\coth^2(|\theta^{(1)}_{\tilde{\omega}}|)$. The contribution from the latter can be reduced by increasing the squeezing parameter $\theta^{(1)}_{\tilde{\omega}}$, which can be achieved by increasing the amplitude α_{p} of the probe or by tuning the central frequencies $\tilde{\omega}, \omega_{\mathrm{p}}$ according to Fig. 4. The state-dependent contribution to the expectation value and the variance above are expressed in terms of the transformed sampled state of the MIR. However, they can be rewritten with respect to the state of the MIR mode $\hat{\rho}_{\tilde{\Omega}}$. Inserting Eq. (34) into the ensemble average and using the definitions $\hat{\vec{\mathfrak{X}}} = [\hat{\mathfrak{X}}_{\mathrm{SA}}(\varphi), \hat{\mathfrak{X}}_{\mathrm{SA}}(-\varphi-\Phi_\perp), \hat{\mathfrak{X}}_{\mathrm{TH}}(-\varphi)]^{\mathrm{T}}$ as well as $\vec{r} = [\mu_{\mathrm{T}}\mu_{\mathrm{S}}, \mu_{\mathrm{T}}|\nu_{\mathrm{S}}|, \nu_{\mathrm{T}}]^{\mathrm{T}}$, the expectation value in Eq. (D1) can be expressed as

$$\left\langle \hat{\mathfrak{X}}_{\mathrm{SA}}(\varphi)\right\rangle_{\hat{\tilde{\rho}}_{\mathrm{SA}}} = \left\langle \vec{r}^{\mathrm{T}}\hat{\vec{\mathfrak{X}}}\right\rangle_{\hat{\rho}_{\tilde{\Omega}}}, \tag{D3}$$

and by defining the quantum covariance matrix,

$$\mathrm{cov}(\hat{\vec{\mathfrak{X}}})|_{\hat{\rho}_{\tilde{\Omega}}} = \frac{1}{2}\Big\langle \Big(\hat{\vec{\mathfrak{X}}} - \langle\hat{\vec{\mathfrak{X}}}\rangle\Big)\Big(\hat{\vec{\mathfrak{X}}} - \langle\hat{\vec{\mathfrak{X}}}\rangle\Big)^{\mathrm{T}} + \Big[\Big(\hat{\vec{\mathfrak{X}}} - \langle\hat{\vec{\mathfrak{X}}}\rangle\Big)\Big(\hat{\vec{\mathfrak{X}}} - \langle\hat{\vec{\mathfrak{X}}}\rangle\Big)^{\mathrm{T}}\Big]^{\mathrm{T}}\Big\rangle_{\hat{\rho}_{\tilde{\Omega}}}, \tag{D4}$$

with the following (i,j)th matrix element $(\mathrm{cov}[\hat{\vec{\mathfrak{X}}}]_{\hat{\rho}_{\tilde{\Omega}}})_{ij} = \frac{1}{2}\langle\{\hat{\mathfrak{X}}_i, \hat{\mathfrak{X}}_j\}\rangle_{\hat{\rho}_{\tilde{\Omega}}} - \langle\hat{\mathfrak{X}}_i\rangle_{\hat{\rho}_{\tilde{\Omega}}}\langle\hat{\mathfrak{X}}_j\rangle_{\hat{\rho}_{\tilde{\Omega}}}$ defined by the ith and jth component of $\hat{\vec{\mathfrak{X}}}$ respectively, the variance can be brought into the form

$$\sigma^2_{\hat{\mathfrak{X}}_{\mathrm{SA}}(\varphi)}|_{\hat{\tilde{\rho}}_{\mathrm{SA}}} = \vec{r}^{\mathrm{T}}\mathrm{cov}(\hat{\vec{\mathfrak{X}}})|_{\hat{\rho}_{\tilde{\Omega}}}\vec{r} = \mathrm{cov}(\vec{r}^{\mathrm{T}}\hat{\vec{\mathfrak{X}}})|_{\hat{\rho}_{\tilde{\Omega}}}. \tag{D5}$$

The first summand of the three contributions to the observable $\vec{r}^{\mathrm{T}}\hat{\vec{\mathfrak{X}}}$ can be understood as follows. Since the refractive index is flat in the MIR range, the phase-matching function in Eq. (4) can be simplified to $\mathrm{sinc}(\eta_{\mathrm{c}}\Omega)$ with $\eta_{\mathrm{c}} = (L/2c)[n_{\mathrm{g}}(\tilde{\omega}) - n(0)]$ depending on the group refractive index $n_{\mathrm{g}}(\tilde{\omega})$ (see Appendix C for details). The spectral function of the sampled mode $f_{\mathrm{SA}}(\Omega)$ is therefore proportional to the probe spectral function modulated by the phase-matching function $\mathrm{sinc}(\eta_{\mathrm{c}}\Omega)$. If $|f_{\mathrm{SA}}(\Omega)|$ (and thus the probe bandwidth σ_{p}) is much broader than $|f_{\tilde{\Omega}}(\Omega)|$, the expectation value can be approximated by

$$\mathrm{tr}\left(\hat{\mathfrak{X}}_{\mathrm{SA}}(\varphi)\hat{\rho}_{\tilde{\Omega}}\right) \underset{\sim}{\propto} \mathrm{tr}\left(\hat{X}_{t_{\mathrm{p}}-\eta_{\mathrm{c}}}(\tilde{\varphi})\hat{\rho}_{\tilde{\Omega}}\right) + \mathrm{tr}\left(\hat{X}_{t_{\mathrm{p}}+\eta_{\mathrm{c}}}(\tilde{\varphi})\hat{\rho}_{\tilde{\Omega}}\right), \tag{D6}$$

with $\tilde{\varphi} = \varphi + \arg[f_{\mathrm{SA}}(\tilde{\Omega})]$ at the central frequency $\tilde{\Omega}$ of the MIR and the instantaneous quadrature $\hat{X}_t(\tilde{\varphi})$ at time t. In the limit case of an ideal classical electro-optic measurement with infinitely short probe pulses, the signal is directly related to the instantaneous quadrature expectation values, since the MIR pulse is sampled over a time slice defined by the probe pulse duration. A small uncertainty in time σ_t will lead to a broader frequency band σ_ω of the probing system (in the present case, the probe E_{p}) due to the Gabor limit $\sigma^2_\omega \ge \pi/(2\sigma^2_t)$ [71]. However, as can be seen from Fig. 3, a broader banded probe pulse will lead to some SFG in addition to the sampled DFG contribution since the higher end of the band is above the filtered frequency $\tilde{\omega}$ but some of the lower end of the band is below $\tilde{\omega}$. This will lead to an increase of the single-mode and two-mode squeezing parameter ζ_{S}, ζ_{T} accounting for the SFG contributions, as can be seen in Fig. 4. The two-mode squeezing creates entanglement between the sampled MIR mode and a temporal mode, which is not sampled and therefore leads

to entanglement breaking which in turn mixes the sampled state and thus increases its von Neumann entropy, which is referred to as thermalization. As will be shown in the following, for a coherent MIR input state $\hat{\rho}_{\tilde{\Omega}}$ (including the vacuum as a limit case), the main result from Ref. [54] can be reproduced using Eq. (D5), which shows that in the squeezing regime, i.e., $\bar{\mathfrak{a}}_{\tilde{\omega}} = \hat{\mathfrak{a}}^{\dagger}_{\tilde{\omega}}$, thermalization leads to an increase of the variance. Expanding Eq. (D5) leads to

$$\begin{aligned}\sigma^2_{\hat{\mathfrak{X}}_{\mathrm{SA}}(\varphi)}|_{\hat{\tilde{\rho}}_{\mathrm{SA}}} &= \vec{r}^{\mathrm{T}}\mathrm{cov}(\hat{\vec{\mathfrak{X}}})|_{\hat{\rho}_{\tilde{\Omega}}}\vec{r} \\ &= \Big\{\mu_{\mathrm{T}}^2\mu_{\mathrm{S}}^2\sigma^2_{\hat{\mathfrak{X}}_{\mathrm{SA}}(\varphi)} + \mu_{\mathrm{T}}^2|\nu_{\mathrm{S}}|^2\sigma^2_{\hat{\mathfrak{X}}_{\mathrm{SA}}(-\varphi-\Phi_\perp)} + \nu_{\mathrm{T}}^2\sigma^2_{\hat{\mathfrak{X}}_{\mathrm{TH}}(-\varphi)} + 2\mu_{\mathrm{T}}^2\mu_{\mathrm{S}}|\nu_{\mathrm{S}}|\mathrm{cov}[\hat{\mathfrak{X}}_{\mathrm{SA}}(\varphi), \hat{\mathfrak{X}}_{\mathrm{SA}}(-\varphi-\Phi_\perp)] \\ &\quad + 2\mu_{\mathrm{T}}\nu_{\mathrm{T}}|\nu_{\mathrm{S}}|\mathrm{cov}[\hat{\mathfrak{X}}_{\mathrm{SA}}(-\varphi-\Phi_\perp), \hat{\mathfrak{X}}_{\mathrm{TH}}(-\varphi)] + 2\mu_{\mathrm{T}}\nu_{\mathrm{T}}\mu_{\mathrm{S}}\mathrm{cov}[\hat{\mathfrak{X}}_{\mathrm{SA}}(\varphi), \hat{\mathfrak{X}}_{\mathrm{TH}}(-\varphi)]\Big\}\Big|_{\hat{\rho}_{\tilde{\Omega}}}. \end{aligned} \tag{D7}$$

If we assume that the reduced density operator $\hat{\rho}_{\tilde{\Omega}}(\hat{a}_{\tilde{\Omega}}) = \hat{\rho}_{\mathrm{SA}}(A_{\mathrm{SA}}\hat{a}_{\mathrm{SA}}) \otimes \hat{\rho}_{\mathrm{TH}}(A_{\mathrm{TH}}\hat{a}_{\mathrm{TH}}) \otimes \hat{\rho}_{\mathrm{U}}(A_{\mathrm{U}}\hat{a}_{\mathrm{U}})$ separates,

$$\begin{aligned}\sigma^2_{\hat{\mathfrak{X}}_{\mathrm{SA}}(\varphi)}|_{\hat{\tilde{\rho}}_{\mathrm{SA}}} &= \Big\{\mu_{\mathrm{T}}^2\Big[\mu_{\mathrm{S}}^2\sigma^2_{\hat{\mathfrak{X}}_{\mathrm{SA}}(\varphi)} + |\nu_{\mathrm{S}}|^2\sigma^2_{\hat{\mathfrak{X}}_{\mathrm{SA}}(-\varphi)}\Big] + \nu_{\mathrm{T}}^2\sigma^2_{\hat{\mathfrak{X}}_{\mathrm{TH}}(-\varphi)} \\ &\quad + \mu_{\mathrm{T}}^2\mu_{\mathrm{S}}|\nu_{\mathrm{S}}|\Big(\Big\langle\{\hat{\mathfrak{X}}_{\mathrm{SA}}(\varphi), \hat{\mathfrak{X}}_{\mathrm{SA}}(-\varphi-\Phi_\perp)\}\Big\rangle - 2\langle\hat{\mathfrak{X}}_{\mathrm{SA}}(\varphi)\rangle\langle\hat{\mathfrak{X}}_{\mathrm{SA}}(-\varphi-\Phi_\perp)\Big\rangle\Big)\Big\}_{\hat{\rho}_{\tilde{\Omega}}}. \end{aligned} \tag{D8}$$

For a coherent state $\hat{\rho}_{\tilde{\Omega}}(\hat{a}_{\tilde{\Omega}}) = \hat{D}_{\tilde{\Omega}}(\alpha_{\tilde{\Omega}})|0\rangle\langle 0|\hat{D}^{\dagger}_{\tilde{\Omega}}(\alpha_{\tilde{\Omega}})$, the variances are

$$\begin{aligned}\sigma^2_{\hat{\mathfrak{X}}_{\mathrm{SA}}(\varphi)}|_{\hat{\tilde{\rho}}_{\mathrm{SA}}} &= \mu_{\mathrm{T}}^2\frac{1}{4}(\mu_{\mathrm{S}}^2 + |\nu_{\mathrm{S}}|^2) + \frac{1}{4}\nu_{\mathrm{T}}^2 + e^{2i\varphi}\mu_{\mathrm{T}}^2\mu_{\mathrm{S}}|\nu_{\mathrm{S}}|\frac{1}{2}\cos(\Phi_\perp) \\ &= \frac{1}{2}\Big\langle\hat{\mathfrak{a}}^{\dagger}_{\tilde{\omega}}\hat{\mathfrak{a}}_{\tilde{\omega}}\Big\rangle \pm \frac{1}{2}\mathrm{Re}(\langle\hat{\mathfrak{a}}^2_{\tilde{\omega}}\rangle) - \frac{1}{4}. \end{aligned} \tag{D9}$$

If $\hat{\mathfrak{X}}_{\mathrm{SA}}(\varphi_X)$ and $\hat{\mathfrak{X}}_{\mathrm{SA}}(\varphi_Y)$ are measured separately and thus $\tilde{s} = -\coth^2(\theta^{(1)}_{\tilde{\omega}})$, the result from Ref. [54] is reproduced. As explained in the main text, it is still possible to mitigate the thermalization noise without compromising on the bandwidth of the probe, by filtering below probe central frequency, i.e., increasing the difference $\tilde{\omega} - \omega_{\mathrm{p}}$, thus sampling less SFG since more of the bandwidth is above the filtered frequency $\tilde{\omega}$. As a result, the single-mode and two-mode squeezing is reduced, which agrees with Fig. 4.

[1] R. E. Slusher, P. Grangier, A. LaPorta, B. Yurke, and M. J. Potasek, *Pulsed squeezed light*, Phys. Rev. Lett. **59**, 2566 (1987).

[2] T. Hirano and M. Matsuoka, *Broadband squeezing of light by pulse excitation*, Opt. Lett. **15**, 1153 (1990).

[3] D. T. Smithey, M. Beck, M. Belsley, and M. G. Raymer, *Sub-shot-noise correlation of total photon number using macroscopic twin pulses of light*, Phys. Rev. Lett. **69**, 2650 (1992).

[4] D. T. Smithey, M. Beck, M. G. Raymer, and A. Faridani, *Measurement of the Wigner distribution and the density matrix of a light mode using optical homodyne tomography: Application to squeezed states and the vacuum*, Phys. Rev. Lett. **70**, 1244 (1993).

[5] D. T. Smithey, M. Beck, J. Cooper, and M. G. Raymer, *Measurement of number-phase uncertainty relations of optical fields*, Phys. Rev. A **48**, 3159 (1993).

[6] A. Zavatta, M. Bellini, P. L. Ramazza, F. Marin, and F. T. Arecchi, *Time-domain analysis of quantum states of light: Noise characterization and homodyne tomography*, J. Opt. Soc. Am. B **19**, 1189 (2002).

[7] A. Zavatta, S. Viciani, and M. Bellini, *Non-classical field characterization by high-frequency, time-domain quantum homodyne tomography*, Laser Phys. Lett. **3**, 3 (2005).

[8] O. Haderka, V. Michálek, V. Urbášek, and M. Ježek, *Fast time-domain balanced homodyne detection of light*, Appl. Opt. **48**, 2884 (2009).

[9] R. Okubo, M. Hirano, Y. Zhang, and T. Hirano, *Pulse-resolved measurement of quadrature phase amplitudes of squeezed pulse trains at a repetition rate of 76 MHz*, Opt. Lett. **33**, 1458 (2008).

[10] J. Tiedau, V. S. Shchesnovich, D. Mogilevtsev, V. Ansari, G. Harder, T. J. Bartley, N. Korolkova, and C. Silberhorn, *Quantum state and mode profile tomography by the overlap*, New J. Phys. **20**, 033003 (2018).

[11] V. Ansari, G. Harder, M. Allgaier, B. Brecht, and C. Silberhorn, *Temporal-mode measurement tomography of a quantum pulse gate*, Phys. Rev. A **96**, 063817 (2017).

[12] V. Ansari, J. M. Donohue, M. Allgaier, L. Sansoni, B. Brecht, J. Roslund, N. Treps, G. Harder, and C. Silberhorn, *Tomography and purification of the temporal-mode structure of quantum light*, Phys. Rev. Lett. **120**, 213601 (2018).

[13] J. Gil-Lopez, Y. S. Teo, S. De, B. Brecht, H. Jeong, C. Silberhorn, and L. L. Sánchez-Soto, *Universal compressive tomography in the time-frequency domain*, Optica **8**, 1296 (2021).
[14] M. Kalash and M. V. Chekhova, *Wigner function tomography via optical parametric amplification*, Optica **10**, 1142 (2023).
[15] R. Yanagimoto, E. Ng, M. Jankowski, R. Nehra, T. P. McKenna, T. Onodera, L. G. Wright, R. Hamerly, A. Marandi, M. M. Fejer, and H. Mabuchi, *Mesoscopic ultrafast nonlinear optics—The emergence of multimode quantum non-Gaussian physics*, Optica **11**, 896 (2024).
[16] J. Gulla, K. Ryen, and J. Skaar, *Limits for realizing single photons*, Phys. Rev. A **108**, 063708 (2023).
[17] C. Weedbrook, S. Pirandola, R. García-Patrón, N. J. Cerf, T. C. Ralph, J. H. Shapiro, and S. Lloyd, *Gaussian quantum information*, Rev. Mod. Phys. **84**, 621 (2012).
[18] S. L. Braunstein and P. van Loock, *Quantum information with continuous variables*, Rev. Mod. Phys. **77**, 513 (2005).
[19] C. Weedbrook, A. M. Lance, W. P. Bowen, T. Symul, T. C. Ralph, and P. K. Lam, *Quantum cryptography without switching*, Phys. Rev. Lett. **93**, 170504 (2004).
[20] A. M. Lance, T. Symul, V. Sharma, C. Weedbrook, T. C. Ralph, and P. K. Lam, *No-switching quantum key distribution using broadband modulated coherent light*, Phys. Rev. Lett. **95**, 180503 (2005).
[21] L. S. Madsen, V. C. Usenko, M. Lassen, R. Filip, and U. L. Andersen, *Continuous variable quantum key distribution with modulated entangled states*, Nat. Commun. **3**, 1083 (2012).
[22] V. C. Usenko and F. Grosshans, *Unidimensional continuous-variable quantum key distribution*, Phys. Rev. A **92**, 062337 (2015).
[23] E. Diamanti and A. Leverrier, *Distributing secret keys with quantum continuous variables: Principle, security and implementations*, Entropy **17**, 6072 (2015).
[24] N. Hosseinidehaj, Z. Babar, R. Malaney, S. X. Ng, and L. Hanzo, *Satellite-based continuous-variable quantum communications: State-of-the-art and a predictive outlook*, IEEE Commun. Surv. Tutor. **21**, 881 (2019).
[25] C. Silberhorn, T. C. Ralph, N. Lütkenhaus, and G. Leuchs, *Continuous variable quantum cryptography: Beating the 3 dB loss limit*, Phys. Rev. Lett. **89**, 167901 (2002).
[26] M. Hillery, *Quantum cryptography with squeezed states*, Phys. Rev. A **61**, 022309 (2000).
[27] K. Vogel and H. Risken, *Determination of quasiprobability distributions in terms of probability distributions for the rotated quadrature phase*, Phys. Rev. A **40**, 2847 (1989).
[28] U. Leonhardt and H. Paul, *High-accuracy optical homodyne detection with low-efficiency detectors: "Preamplification" from antisqueezing*, Phys. Rev. Lett. **72**, 4086 (1994).
[29] S. Wallentowitz and W. Vogel, *Unbalanced homodyning for quantum state measurements*, Phys. Rev. A **53**, 4528 (1996).
[30] G. Breitenbach, S. Schiller, and J. Mlynek, *Measurement of the quantum states of squeezed light*, Nature (London) **387**, 471 (1997).
[31] A. Luis, J. Sperling, and W. Vogel, *Nonclassicality phase-space functions: More insight with fewer detectors*, Phys. Rev. Lett. **114**, 103602 (2015).
[32] M. Bohmann, J. Tiedau, T. Bartley, J. Sperling, C. Silberhorn, and W. Vogel, *Incomplete detection of nonclassical phase-space distributions*, Phys. Rev. Lett. **120**, 063607 (2018).
[33] E. Knyazev, K. Y. Spasibko, M. V. Chekhova, and F. Y. Khalili, *Quantum tomography enhanced through parametric amplification*, New J. Phys. **20**, 013005 (2018).
[34] S. Olivares, A. Allevi, G. Caiazzo, M. G. A. Paris, and M. Bondani, *Quantum tomography of light states by photon-number-resolving detectors*, New J. Phys. **21**, 103045 (2019).
[35] N. G. Walker and J. E. Carroll, *Multiport homodyne detection near the quantum noise limit*, Opt. Quantum Electron. **18**, 355 (1986).
[36] M. Freyberger, K. Vogel, and W. P. Schleich, *From photon counts to quantum phase*, Phys. Lett. A **176**, 41 (1993).
[37] U. Leonhardt and H. Paul, *Realistic optical homodyne measurements and quasiprobability distributions*, Phys. Rev. A **48**, 4598 (1993).
[38] A. Zucchetti, W. Vogel, and D.-G. Welsch, *Quantum-state homodyne measurement with vacuum ports*, Phys. Rev. A **54**, 856 (1996).
[39] J. Řeháček, Y. S. Teo, Z. Hradil, and S. Wallentowitz, *Surmounting intrinsic quantum-measurement uncertainties in Gaussian-state tomography with quadrature squeezing*, Sci. Rep. **5**, 12289 (2015).
[40] F. S. Roux and N. Fabre, *Wigner functional theory for quantum optics*, arXiv:1901.07782.
[41] F. S. Roux, *Erratum: Combining spatiotemporal and particle-number degrees of freedom* [Phys. Rev. A **98**, 043841 (2018)]; **101**, 019903(E) (2020).
[42] S. Namba, *Electro-optical effect of zincblende*, J. Opt. Soc. Am. **51**, 76 (1961).
[43] G. Gallot and D. Grischkowsky, *Electro-optic detection of terahertz radiation*, J. Opt. Soc. Am. B **16**, 1204 (1999).
[44] A. Leitenstorfer, S. Hunsche, J. Shah, M. C. Nuss, and W. H. Knox, *Detectors and sources for ultrabroadband electro-optic sampling: Experiment and theory*, Appl. Phys. Lett. **74**, 1516 (1999).
[45] P. Sulzer, K. Oguchi, J. Huster, M. Kizmann, T. L. M. Guedes, A. Liehl, C. Beckh, A. S. Moskalenko, G. Burkard, D. V. Seletskiy, and A. Leitenstorfer, *Determination of the electric field and its Hilbert transform in femtosecond electro-optic sampling*, Phys. Rev. A **101**, 033821 (2020).
[46] A. S. Moskalenko, C. Riek, D. V. Seletskiy, G. Burkard, and A. Leitenstorfer, *Paraxial theory of direct electro-optic sampling of the quantum vacuum*, Phys. Rev. Lett. **115**, 263601 (2015).
[47] T. L. M. Guedes, M. Kizmann, D. V. Seletskiy, A. Leitenstorfer, G. Burkard, and A. S. Moskalenko, *Spectra of ultrabroadband squeezed pulses and the finite-time Unruh-Davies effect*, Phys. Rev. Lett. **122**, 053604 (2019).
[48] M. Kizmann, T. L. M. Guedes, D. V. Seletskiy, A. S. Moskalenko, A. Leitenstorfer, and G. Burkard, *Subcycle squeezing of light from a time flow perspective*, Nat. Phys. **15**, 960 (2019).
[49] I.-C. Benea-Chelmus, F. F. Settembrini, G. Scalari, and J. Faist, *Electric field correlation measurements on the electromagnetic vacuum state*, Nature (London) **568**, 202 (2019).

[50] F. Lindel, R. Bennett, and S. Y. Buhmann, *Theory of polaritonic quantum-vacuum detection*, Phys. Rev. A **102**, 041701(R) (2020).

[51] F. Lindel, R. Bennett, and S. Y. Buhmann, *Macroscopic quantum electrodynamics approach to nonlinear optics and application to polaritonic quantum-vacuum detection*, Phys. Rev. A **103**, 033705 (2021).

[52] S. Virally, P. Cusson, and D. V. Seletskiy, *Enhanced electro-optic sampling with quantum probes*, Phys. Rev. Lett. **127**, 270504 (2021).

[53] C. Beckh, P. Sulzer, N. Fritzsche, C. Riek, and A. Leitenstorfer, *Analysis of subcycle electro-optic sampling without background*, J. Infrared Millimeter Terahertz Waves **42**, 701 (2021).

[54] S. Onoe, T. L. M. Guedes, A. S. Moskalenko, A. Leitenstorfer, G. Burkard, and T. C. Ralph, *Realizing a rapidly switched Unruh-DeWitt detector through electro-optic sampling of the electromagnetic vacuum*, Phys. Rev. D **105**, 056023 (2022).

[55] M. Kizmann, A. S. Moskalenko, A. Leitenstorfer, G. Burkard, and S. Mukamel, *Quantum susceptibilities in time-domain sampling of electric field fluctuations*, Laser Photonics Rev. **16**, 2100423 (2022).

[56] T. L. M. Guedes, I. Vakulchyk, D. V. Seletskiy, A. Leitenstorfer, A. S. Moskalenko, and G. Burkard, *Back action in quantum electro-optic sampling of electromagnetic vacuum fluctuations*, Phys. Rev. Res. **5**, 013151 (2023).

[57] F. F. Settembrini, F. Lindel, A. M. Herter, S. Y. Buhmann, and J. Faist, *Detection of quantum-vacuum field correlations outside the light cone*, Nat. Commun. **13**, 3383 (2022).

[58] F. Lindel, A. Herter, V. Gebhart, J. Faist, and S. Y. Buhmann, *Entanglement harvesting from electromagnetic quantum fields*, Phys. Rev. A **110**, 022414 (2024).

[59] F. Lindel, A. M. Herter, J. Faist, and S. Y. Buhmann, *Probing vacuum field fluctuations and source radiation separately in space and time*, Phys. Rev. Res. **5**, 043207 (2023).

[60] O. Schubert, M. Hohenleutner, F. Langer, B. Urbanek, C. Lange, U. Huttner, D. Golde, T. Meier, M. Kira, S. W. Koch, and R. Huber, *Sub-cycle control of terahertz high-harmonic generation by dynamical Bloch oscillations*, Nat. Photonics **8**, 119 (2014).

[61] F. Langer, M. Hohenleutner, C. P. Schmid, C. Poellmann, P. Nagler, T. Korn, C. Schüller, M. S. Sherwin, U. Huttner, J. T. Steiner, S. W. Koch, M. Kira, and R. Huber, *Lightwave-driven quasiparticle collisions on a subcycle timescale*, Nature (London) **533**, 225 (2016).

[62] M. Hangyo, M. Tani, and T. Nagashima, *Terahertz time-domain spectroscopy of solids: a review*, Int. J. Infrared Millimeter **26**, 1661 (2005).

[63] I. Pupeza, M. Huber, M. Trubetskov, W. Schweinberger, S. A. Hussain, C. Hofer, K. Fritsch, M. Poetzlberger, L. Vamos, E. Fill, T. Amotchkina, K. V. Kepesidis, A. Apolonski, N. Karpowicz, V. Pervak, O. Pronin, F. Fleischmann, A. Azzeer, M. Žigman, and F. Krausz, *Field-resolved infrared spectroscopy of biological systems*, Nature (London) **577**, 52 (2020).

[64] C. Riek, D. V. Seletskiy, A. S. Moskalenko, J. F. Schmidt, P. Krauspe, S. Eckart, S. Eggert, G. Burkard, and A. Leitenstorfer, *Direct sampling of electric-field vacuum fluctuations*, Science **350**, 420 (2015).

[65] C. Riek, P. Sulzer, M. Seeger, A. S. Moskalenko, G. Burkard, D. V. Seletskiy, and A. Leitenstorfer, *Subcycle quantum electrodynamics*, Nature (London) **541**, 376 (2017).

[66] E. Hubenschmid, T. L. M. Guedes, and G. Burkard, *Complete positive operator-valued measure description of multichannel quantum electro-optic sampling with monochromatic field modes*, Phys. Rev. A **106**, 043713 (2022).

[67] P. Busch, P. Lahti, and R. F. Werner, *Measurement uncertainty relations*, J. Math. Phys. (N.Y.) **55**, 042111 (2014).

[68] R. F. Werner, *Uncertainty relations for general phase spaces*, Front. Phys. **11**, 110305 (2016).

[69] R. F. Werner and T. Farrelly, *Uncertainty from Heisenberg to today*, Found. Phys. **49**, 460 (2019).

[70] S. Virally and B. Reulet, *Unidimensional time-domain quantum optics*, Phys. Rev. A **100**, 023833 (2019).

[71] D. Gabor, *Theory of communication. Part 1: The analysis of information*, J. Inst. Electr. Eng. **93**, 429 (1946).

[72] R. W. Boyd, *Nonlinear Optics* (Elsevier Science and Technology, Amsterdam, 2019).

[73] M. Hillery, *Sum and difference squeezing of the electromagnetic field*, Phys. Rev. A **40**, 3147 (1989).

[74] P. Sharapova, A. M. Pérez, O. V. Tikhonova, and M. V. Chekhova, *Schmidt modes in the angular spectrum of bright squeezed vacuum*, Phys. Rev. A **91**, 043816 (2015).

[75] P. R. Sharapova, G. Frascella, M. Riabinin, A. M. Pérez, O. V. Tikhonova, S. Lemieux, R. W. Boyd, G. Leuchs, and M. V. Chekhova, *Properties of bright squeezed vacuum at increasing brightness*, Phys. Rev. Res. **2**, 013371 (2020).

[76] K. E. Cahill and R. J. Glauber, *Density operators and quasiprobability distributions*, Phys. Rev. **177**, 1882 (1969).

[77] H. J. Carmichael, *Statistical Methods in Quantum Optics 1* (Springer-Verlag, Berlin, 1999), p. 110.

[78] W. Vogel and D.-G. Welsch, *Quantum Optics* (Wiley-VCH Verlag, Weinheim, 2006), p. 128.

[79] G. Yang, M. Kizmann, A. Leitenstorfer, and A. S. Moskalenko, *Subcycle tomography of quantum light*, arXiv:2307.12812.

[80] S. Onoe, S. Virally, and D. V. Seletskiy, *Direct measurement of the Husimi-Q function of the electric-field in the time-domain*, arXiv:2307.13088.

[81] N. Lordi, E. J. Tsao, A. J. Lind, S. A. Diddams, and J. Combes, *A quantum theory of temporally mismatched homodyne measurements with applications to optical frequency comb metrology*, Phys. Rev. A **109**, 033722 (2024).

[82] R. J. Glauber, *Quantum Theory of Optical Coherence* (Wiley-VCH, Weinheim, 2007), p. 656.

[83] D. T. F. Marple, *Refractive index of* ZnSe, ZnTe, *and* CdTe, J. Appl. Phys. **35**, 539 (1964).